

Analytic solutions to the central-spin problem for nitrogen-vacancy centers in diamondL. T. Hall,^{1,*} J. H. Cole,² and L. C. L. Hollenberg¹¹*Centre for Quantum Computation and Communication Technology, School of Physics, University of Melbourne, Victoria 3010, Australia*²*Chemical and Quantum Physics, School of Applied Sciences, RMIT University, Melbourne 3001, Australia*

(Received 10 October 2013; revised manuscript received 12 June 2014; published 18 August 2014)

Due to interest in both solid-state-based quantum computing architectures and the application of quantum mechanical systems to nanomagnetometry, there has been considerable recent attention focused on understanding the microscopic dynamics of solid-state spin baths and their effects on the coherence of a controllable, coupled central electronic spin. Using a systematic approach based on the spatial statistics of the spin-bath constituents, we develop a detailed, purely analytic theory for the central-spin decoherence problem of a nitrogen-vacancy center electron coupled to its native 1.1% bath of ¹³C nuclear spins. Our theory reproduces the experimental and numerical results found in the literature, and provides a detailed theoretical description of the relevant decoherence profiles, their associated rates, corresponding electron spin-echo envelope modulations features, and an explicit analytic account of why the strength of an applied magnetic field has such a profound effect on the coherence time of the central spin.

DOI: [10.1103/PhysRevB.90.075201](https://doi.org/10.1103/PhysRevB.90.075201)

PACS number(s): 76.60.Lz, 75.40.Gb, 76.30.Mi

I. INTRODUCTION

The central-spin problem refers to a special class of open quantum systems, in which a central spin (S) interacts with a large number of strongly coupled spins in the environment (E), as depicted in Fig. 1. This results in an irreversible loss of quantum information from the central system, as quantified by the decay of phase coherence between its corresponding basis states, such that certain elements of the system are no longer able to interfere with each other. In the case of pure dephasing processes, for which there is no energy transfer between the system and the environment, this results in a damping of the off-diagonal terms of the associated reduced density matrix of S,

$$\text{Tr}_E\{\rho(t)\}_{ij} = L_{ij}\text{Tr}_E\{\rho(0)\}_{ij}, \quad (1)$$

where $\text{Tr}_E\{\dots\}$ denotes a trace over the environmental degrees of freedom of the density matrix ρ , $L_{ij} = \exp[-\Lambda_{ij}(t)]$ is often referred to as the decoherence envelope, and Λ_{ij} as the decoherence function. It is the derivation of these quantities in the context of the central-spin problem with which we concern ourselves in this work.

This problem has received renewed attention over the last decade, due in no small part to localized electrons in solids being promising candidates for qubits in quantum computation, metrology, and communication systems, a result of their long coherence times, ease of quantum control, and already well-established fabrication techniques. In the context of quantum information processing, the utility of these systems hinges upon the requirement for spin coherence times to be sufficiently long to ensure that the necessary number of quantum operations [1] can be performed within the associated coherence time. Examples of such systems that have been suggested as building blocks for quantum computer architectures include spins qubits in quantum dots [2,3], donor impurities [4–7], and nitrogen-vacancy (NV) centers in diamond [8]. In the context of metrology, with particular

regard to parameter estimation, the NV center has emerged as a unique physical platform for nanoscale magnetometry [9–13], nano-NMR [14–16], bioimaging [17–19], electrometry [20], thermometry [21], and decoherence imaging [22–26]. In each case, the associated sensitivity is ultimately limited by the coherence properties of the NV spin that arise from the strong coupling to the surrounding bath of electron and/or nuclear spins. In all of these applications and platforms, a comprehensive understanding of the central-spin problem is therefore necessary to make accurate predictions of the quantum properties and behavior of the central spin arising from the material properties of the surrounding environment.

The first modern approach to this problem, in the context of phosphorus donors in silicon, involved treating the combined effect of the spin-bath environment on the central spin as a semiclassical magnetic field whose dynamic properties were intended to mimic the magnetic dipole flip-flop processes taking place amongst the environmental spins [27,28], and has since found considerable application in the NV community [10,29–34]. This approach, however, does not account for the effect of the central spin on the surrounding environment, restricting its application to cases in which environmental spin-spin interactions are significantly stronger than couplings between the environment and the central spin (as is the case with NV centers in diamond nanocrystals [26], for example). In order to account for the full interaction between the central spin and its environment, quantum cluster expansion [35–37], nuclear pairwise [38–40], correlated cluster expansion [41,42], and disjoint cluster expansion [30] models have been developed, in which the environment is systematically clustered into groups of strongly interacting spins, with each order of the cluster hierarchy corresponding to successively weaker, and hence less important, interactions.

The nitrogen-vacancy (NV) center (see Ref. [43] for an extensive review) is a point defect in a diamond lattice comprised of a substitutional atomic nitrogen impurity and an adjacent crystallographic vacancy [Fig. 2(a)]. The energy level scheme of the C_{3v} -symmetric NV system [Fig. 2(b)] consists of ground (³A), excited (³E), and metastable (¹A) electronic states. The ground-state spin-1 manifold has three

*lthall@physics.unimelb.edu.au

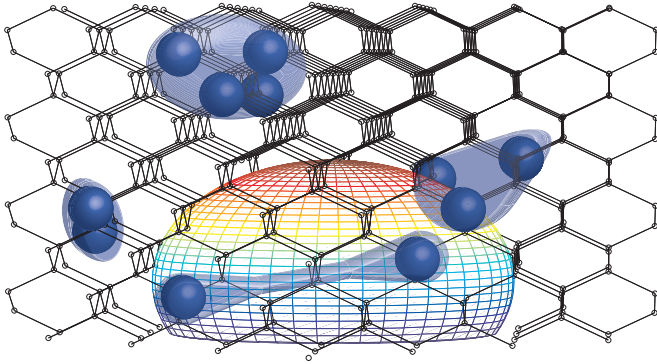


FIG. 1. (Color online) Schematic of the central-spin problem showing a central spin coupled to clusters of randomly distributed environmental spins. The large central sphere represents the region concentric on the central spin inside which we expect to find, on average, less than one environmental spin.

spin sublevels ($|0\rangle, |\pm 1\rangle$), which in zero field are split by 2.88 GHz. An important property of the NV system is that under optical excitation the spin levels are distinguishable by a difference in fluorescence, hence, spin-state readout is achieved by purely optical means [44,45]. The degeneracy between the $|\pm 1\rangle$ states may be lifted with the application of a background field, with a corresponding separation of 17.6 MHz G^{-1} permitting all three states to be accessible via microwave control, however, the $|\pm 1\rangle$ states are not directly distinguishable from one another via optical means. By isolating either the $|0\rangle \leftrightarrow |+1\rangle$ or $|0\rangle \leftrightarrow |-1\rangle$ transitions, the NV spin system constitutes a controllable, addressable spin qubit.

The large zero-field splitting is fortuitous in the present context, in that it renders typical NV-environment spin-spin couplings (of roughly MHz) unable to cause transitions in the ground-state spin-triplet manifold. While the weak spin-orbit coupling to crystal phonons (and low phonon density, owing to the large Debye temperature of diamond) leads to longitudinal relaxation of the spin state on time scales of roughly $T_1 \sim 10$ ms at room temperature, the lateral relaxation (T_2) of the NV spin is determined by the dipole-dipole coupling to other spin impurities in the diamond crystal and can occur on time

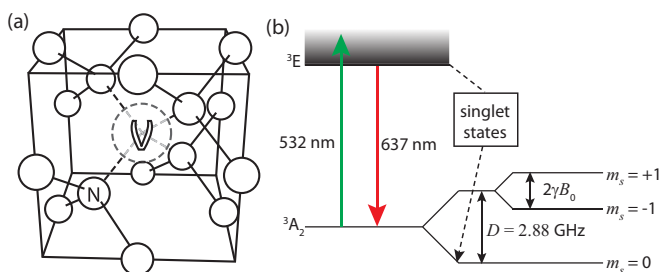


FIG. 2. (Color online) (a) The nitrogen-vacancy (NV) center point defect in a diamond lattice, comprised of a substitutional atomic nitrogen impurity (N) and an adjacent crystallographic vacancy (V). (b) The NV ground state spin sublevels are separated by $D = 2.87$ GHz. Upon optical excitation at 532 nm, the population of the $|0\rangle$ state may be readout by monitoring the intensity of the emitted red light.

scales of 0.1–1 μs in naturally occurring type-1b diamond. Such coherence times may be greatly extended with the use of higher-grade diamond crystal, or with the application of spin-echo [46] or higher-order dynamic decoupling sequences to suppress the effect of the surrounding spin bath on the NV spin. For example, the use of “ultrapure” diamond crystal with parts-per-billion (ppb) concentrations of nitrogen electron donor impurities (as compared with naturally occurring concentrations of parts-per-million or more) leads to ^{13}C nuclear spin limited spin-echo coherence times of $T_2 \sim 100 \mu s - 1$ ms. Such results are by no means fundamental, however, and may be further improved with the use of isotopically pure diamond crystal with reduced ^{13}C concentrations [11]. As such, T_2 may, at least in principle, be as long as the longitudinal relaxation time T_1 . These relatively narrow spectral properties of the NV⁻ ground state, together with its room-temperature operation and optical readout, make it an ideal candidate for both single spin-based magnetometry and electrometry. As such, the NV spin coupled to a surrounding bath of ^{13}C nuclear spins of natural abundance (1.1%) is the primary physical system with which we concern ourselves for this study.

Traditionally, the theoretical analysis of the central-spin problem has been based on phenomenological assumptions regarding the self-interaction dynamics of the surrounding spin bath, namely, by replacing the bath with a classical Ornstein-Uhlenbeck noise source [47,48]. This noise gives rise to fluctuations in the Larmor frequency of the central spin and leads to an eventual dephasing between its initially coherent basis states, a process referred to as spectral diffusion. Such approaches ignore the influence of the central spin on the surrounding environment, and require *ad hoc* assumptions regarding the decaying exponential form for the autocorrelation function of the effective magnetic dipole field $\langle B(t)B(t') \rangle \sim \langle B^2 \rangle \exp(-|t - t'|/T_c)$, with the decay rate being deduced from the effective environmental flip-flop rates [27,28]. This assumption of a linear exponential decay gives rise to a cubic exponential decay in the coherence of the central spin under a spin-echo pulse sequence for times shorter than the autocorrelation time (see Ref. [49] for a review). In this work, we show that a magnetization conserving two spin flip-flop models must have an autocorrelation function with zero derivative at $t = t'$, which cannot be satisfied by a function of this form.

One of the earliest modern attempts at deriving the autocorrelation time from consideration of microscopic physical processes was given in Ref. [28]. Here, each magnetic dipole coupled nuclear spin pair (consisting of spins m and n) was treated as a bistable fluctuator, where the number of transitions between states in a given time interval t is treated as a Poissonian variable with parameter t/T_{mn} . The effective flip-flop rate of the pair $1/T_{mn}$ could then be calculated using their mutual dipolar coupling strength via perturbation theory, resulting in a linear exponential decay of the autocorrelation function. However, this still requires certain phenomenological assumptions to be made about the associated density of states, and does not address the microscopic reasons behind how the T_{mn} quantities are distributed. Adopting this approach in the context of NV based quantum sensing applications would mean that, for a given T_2 measurement of a NV spin coupled to its native bath of ^{13}C spins, one would be led to infer that the

associated correlation time of the environment is three orders of magnitude longer than its true value. As an example, using the treatment of the nuclear spin bath in Ref. [10], typical coherence times of $T_2^* = 1 \mu\text{s}$ and $T_2 = 300 \mu\text{s}$ would imply a correlation time of $T_c = T_2^3/[6(T_2^*)^2] = 4.5 \text{ s}$. This is in stark contrast to what would be expected from an examination of the average nuclear-nuclear coupling strength of $1/nb \sim 40 \text{ ms}$, based on an average impurity density $n \approx 2 \text{ nm}^{-3}$, and indeed the correlation times of $T_c \approx 10 \text{ ms}$ calculated in this work. These problems are addressed and clarified in what follows, as our results show that the spatial distribution of spins around the central spin has a significant effect on the analytic form of the autocorrelation function and, subsequently, that of the resulting decoherence functions. This is critical to the development of spin-based quantum technologies, as there have been many quantitative predictions of better performance with the use of pulse-based microwave control schemes [10,13,50], and the exact analytic form of the spectral cutoff was shown to directly affect the performance of such schemes [51,52].

In this work, we show that this discrepancy arises from ignoring the backaction of the environment on the central spin. This simplification can only be made when the interaction strengths between the environmental constituents far exceed the interaction between the central spin and this environment. Such a regime is characterised by a very dense distribution of environmental spins, while having the central spin exist at a relatively large spatial separation from this distribution, as is the case when using the NV to sense dense, external environments [24–26], or for the case of a central nuclear spin coupled to a bath of electron spins. When such a regime is realized, correlations within the environment decay before the influence of the central spin can have any effect, meaning the latter can be ignored. This is not the case for a NV center coupled to the naturally occurring 1.1% ^{13}C nuclear spin bath in diamond. Cases in which these couplings are of similar magnitude, as with the P1 electron bath of type-1b diamond, fall somewhere between these two limits, and are thus beyond the scope of this work.

In response to the limitations of semiclassical models, fully quantum mechanical approaches to the problem have been developed in the last decade using cluster expansion [35–37] and correlated cluster expansion [41,42] methods. In the case of the former, the randomly distributed spins are aggregated into small, strongly interacting groups, meaning this method is well suited to sparse distributions. The latter method shows better convergence in cases where bath sites are densely populated with impurities, or where the decoherence time of the central spin is comparable to, or longer than, the autocorrelation time of the environment, as is the case with a bath of electron spins. In the opposite regime, as would be the case for an electron spin coupled to a nuclear spin bath, these two approaches agree, and to lowest nontrivial order they are in accordance with earlier nuclear pair-correlation approaches [38–40]. In this limit, at least for short times ($t \ll T_2$), all of these approaches are shown to be consistent with a quartic-exponential decay, the likes of which may also be deduced using a generalized semiclassical argument [23]. The numerical work in Ref. [35] shows that numerical computation of the combined effect of many randomly distributed nuclear spin clusters leads to an approximately Gaussian decay of coherence in phosphorous

donor electron spins in silicon on time scales of $t \sim T_2$, the likes of which have also been observed experimentally in NV spins in ultrapure diamond [53]. In this work, we derive the analytic forms of the decoherence functions on all relevant time scales, showing agreement with the $t \ll T_2$ and $t \sim T_2$ limits noted above.

In cases of relatively strong hyperfine interactions resulting from low magnetic field regimes, direct dipole-dipole couplings are either treated as a perturbation [37,54], or ignored completely [55–58]. We note that such approaches are not applicable to the system studied here, as the NV spin spends an appreciable amount of time in its $|0\rangle$ state, during which the hyperfine interaction is effectively turned off. This, in turn, means that environmental spins are free to evolve exclusively under their mutual couplings, and information previously encoded onto them from the central via the hyperfine interaction is free to propagate throughout the environment (see Fig. 3). Despite the techniques developed in the above references not being relevant to the NV- ^{13}C system, it is important to appreciate the distinction between what is meant by “low field” in the context of the Ga:As and P:Si systems mentioned within, and that of the system studied here. In the case of the former, the dominant interaction between environmental constituents is due to hyperfine-mediated flip flops, resulting from environmental spins becoming increasingly coupled to the lateral components of the central spin with decreasing magnetic field strength. This is a consequence of the Zeeman energies of the central electron approaching that of the surrounding nuclei, meaning the two are able to exchange magnetization with appreciable probability. Such effects are negligible in the case of NV centers in diamond, owing to its 2.88-GHz zero-field splitting. Here, the strength of the magnetic field determines whether

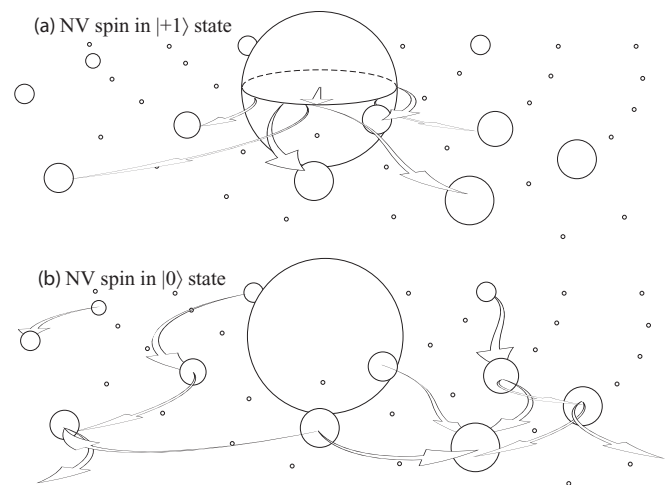


FIG. 3. Schematic depicting the two-step process of NV spin decoherence. In the first step (a), the NV spin is in its $|+1\rangle$ state, and quantum information regarding the NV spin state is imparted onto the environmental nuclear spins via the hyperfine interaction. This process is effectively reversible, as the nuclei cannot interact due to the strong hyperfine field of the NV. When the NV spin is flipped into its $|0\rangle$ state (b), the hyperfine coupling is turned off and this information is free to propagate throughout the lattice via the nuclear dipole-dipole interaction, rendering its loss irreversible.

the quantization axis of a given bath spin is determined by its Zeeman interaction, or by its coupling to other spins. This distinction that has a dramatic on the bath dynamics, and hence the decoherence properties of the NV spin.

Finally, we remark that any short-time expansion is only valid for times shorter than the reciprocal of the strongest dipolar coupling frequencies in the system, and of particular concern is that any two spins can be found arbitrarily close together (or effectively so on the length scales of the system), making an expansion in low orders of these couplings diverge. In this limit, it is the dipolar interaction between environmental spins that sets their quantization axis, not the Zeeman interaction, invalidating the assumption of each cluster's magnetization being conserved with respect to the global z axis. This is another instance where consideration of the spatial distribution of spin impurities becomes important, and despite being able to describe the decoherence in the compact forms given by the works described above, no discussion has been made regarding the statistical distributions of the spin-spin coupling strengths. Instead, one is forced to resort to Monte Carlo based numerics at this point. The possible outcomes for various realizations of spatial distributions of spin impurities for the case of a NV center coupled to a nuclear spin bath have been numerically investigated in Refs. [30,59,60], and that for electron donors and quantum dots in silicon in Ref. [60]. An extensive numerical study of the dependence of the coherence properties of a NV center on the strength of the applied background magnetic field was conducted in Ref. [59], taking both realistic hyperfine distributions and environmental spin-spin interactions into account. In what follows, we present a fully analytic, quantum mechanical description of the effects of the entire range of magnetic field strengths on a central spin coupled to a completely randomly distributed spin bath. Not only do our results demonstrate remarkable agreement with those of Ref. [59], we also analytically explain many decoherence features within, such as the magnetic field dependence of NV decoherence envelopes and associates electron spin-echo envelope modulations (ESEEM) features.

II. THEORETICAL BACKGROUND

The Hamiltonian describing this system is given by

$$\mathcal{H} = \mathcal{H}_S + \mathcal{H}_{SE} + \mathcal{H}_{EZ} + \mathcal{H}_{EE}, \quad (2)$$

where \mathcal{H}_S is the self-Hamiltonian of the central electron spin, which may include the coupling of the NV spin to its proximate nitrogen nuclear spin, as well as zero field and Zeeman splittings. The hyperfine interaction between the central spin (S) and the environment (E) is described by \mathcal{H}_{SE} , which in the present context is a point-dipole interaction, but may also include Fermi-contact interactions in other systems. This is described by

$$\mathcal{H}_{SE} = \sum_i \frac{a}{R_i^3} \left[\vec{S} \cdot \vec{\mathcal{E}}_i - 3 \frac{(\vec{S} \cdot \mathbf{R}_i)(\mathbf{R}_i \cdot \vec{\mathcal{E}}_i)}{R_i^2} \right], \quad (3)$$

where \vec{S} and $\vec{\mathcal{E}}_i$ are the spin-vector operators for the NV spin and the i th environmental spin, \mathbf{R}_i is their mutual separation, and $a = \frac{\mu_0}{4\pi\hbar} \mu_S \mu_E$. The magnetic moments of the NV and environmental spins are denoted μ_S and μ_E , respectively. The

large zero-field splitting is some three orders of magnitude greater than any other coupling in this system, allowing us to ignore any coupling to the lateral components (\mathcal{S}_x and \mathcal{S}_y) of the NV spin.

The Zeeman (Z) interaction of the environmental spins is described by $\mathcal{H}_{EZ} = \sum_i \vec{\mathcal{E}}_i \cdot \vec{\omega}_i$, where $\vec{\omega}_i = \gamma_E \mathbf{B}_0$ describes the Zeeman field felt by spin i , having gyromagnetic ratio $\gamma_E = \mu_E/\hbar$, due to a background field \mathbf{B}_0 .

The nuclear spin-spin interactions (E) are described by

$$\mathcal{H}_{EE} = \sum_{j<i} \frac{b}{r_{ij}^3} \left[\vec{\mathcal{E}}_i \cdot \vec{\mathcal{E}}_j - 3 \frac{(\vec{\mathcal{E}}_i \cdot \mathbf{r}_{ij})(\mathbf{r}_{ij} \cdot \vec{\mathcal{E}}_j)}{r_{ij}^2} \right], \quad (4)$$

where \mathbf{r}_{ij} is the mutual separation of spins i and j , and $b = \frac{\mu_0}{4\pi\hbar} \mu_E^2$.

In the case of large Zeeman couplings, some transitions between environmental spin states due to the hyperfine and dipolar interactions will be disallowed due to energy conservation, ensuring that the total axial magnetization of the spins involved in the interaction is conserved. However, at low fields, the energy cost for these transitions may be easily paid for by these interactions, meaning that axial magnetization need not be conserved. In what follows, we refer to (non)axial magnetization conserving transitions as being “(non)axial.”

For a given spin \mathcal{E}_i , we may classify its parameter regime in terms of the relative strengths of the energy scales considered above: spin-environment coupling (S), environment self-coupling (E), and Zeeman splitting (Z), as determined by the Hamiltonian components \mathcal{H}_{SE} , \mathcal{H}_{ZE} , and \mathcal{H}_{EE} , respectively. This gives rise to six distinct parameter regimes, as summarized below, and depicted schematically in Fig. 4, and parametrically in Figs. 6 and 7 for various examples of physical systems.

For the sake of brevity, we label these six regions according to the relative strengths of the environmental couplings. For example, a label of ZSE (read $Z > S > E$) would imply that both S-E and E-E couplings are secular (a consequence of their quantization axis being set by the Zeeman field), and that the spins couple more strongly to the NV than to each other. Conversely, a label of ESZ would imply that both S-E and E-E couplings are nonsecular, and that the spins couple more strongly to each other than to the NV (see Fig. 5). The geometric boundaries on these regimes are summarized in the following.

In the ZSE regime, the nuclei are sufficiently far from both the NV and each other that the Zeeman interaction dominates over both the hyperfine and dipolar interactions, ensuring that both classes of interactions must conserve axial magnetization. The $\langle \mathcal{H}_{ZE}^2 \rangle \gg \langle \mathcal{H}_{SE}^2 \rangle \gg \langle \mathcal{H}_{EE}^2 \rangle$ condition yields the following constraints on the geometry of the cluster:

$$\left(\frac{a}{\omega}\right)^{1/3} \leq R \leq r \left(\frac{a}{b}\right)^{1/3}, \\ R \left(\frac{b}{a}\right)^{1/3} \leq r < \infty.$$

Clusters in the SZE regime are sufficiently close to the NV to ensure that the hyperfine coupling dominates over the Zeeman interaction, however, the associated nuclei are still far enough apart to ensure that the Zeeman interaction is larger than

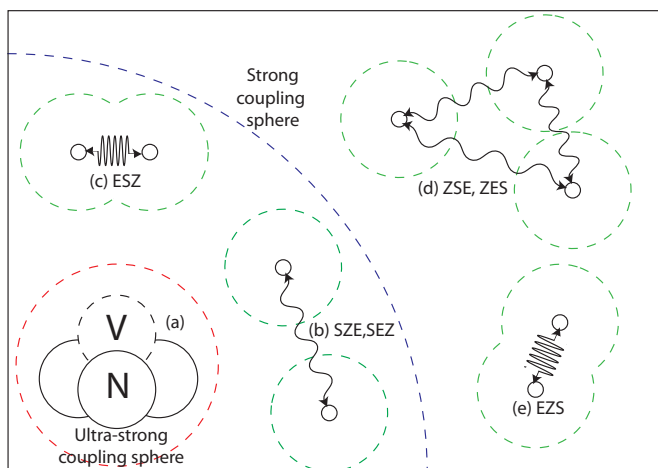


FIG. 4. (Color online) Schematic showing the parameter regimes relevant to the central-spin problem. (a) Ultrastrong coupling region, in which the interaction between the NV center and an adjacent spin is stronger than its 2.88-GHz zero-field splitting. This region is not considered in this work. (b), (c) Strong coupling region, in which the coupling of the spins to the NV center is stronger than their coupling to a background field. In (b), the spins are weakly coupled to each other and are representative of two possible regimes: SEZ and SZE. In (c), the spins are strongly coupled to each other and thus represent the ESZ regime. (d), (e) Weak coupling region, in which the coupling of the spins to a background field is greater than their coupling to the NV. In (d), the spins are weakly coupled to each other and hence represent the ZSE and ZES regimes. In (e), the spins are strongly coupled to each other and represent the EZS regime.

their mutual dipolar coupling. The $\langle \mathcal{H}_{SE}^2 \rangle \gg \langle \mathcal{H}_{ZE}^2 \rangle \gg \langle \mathcal{H}_{EE}^2 \rangle$ condition ensures that

$$0 \leq R \leq \left(\frac{a}{\omega}\right)^{1/3}, \quad \left(\frac{b}{\omega}\right)^{1/3} \leq r < \infty.$$

Clusters in the SEZ regime are both sufficiently tightly bound and close to the NV to ensure that both hyperfine and dipolar couplings dominate over the Zeeman interaction, however, the associated nuclei are still far enough apart to ensure that the hyperfine interaction is larger than their mutual dipolar coupling. The $\langle \mathcal{H}_{SE}^2 \rangle \gg \langle \mathcal{H}_{EE}^2 \rangle \gg \langle \mathcal{H}_{ZE}^2 \rangle$ condition ensures

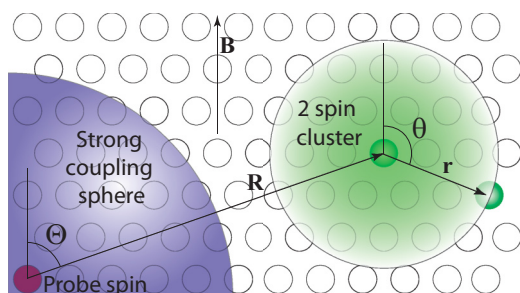


FIG. 5. (Color online) Schematic representation of a two-spin cluster coupled to a central spin. The separation vector between the cluster and the central spin is defined by the location of the closest spin \mathbf{R} . The structure of the cluster is defined by the separation vector(s) of the cluster constituents \mathbf{r} . Evaluation of the ensemble-averaged quantities requires integration over \mathbf{R} , and averaging over \mathbf{r} .

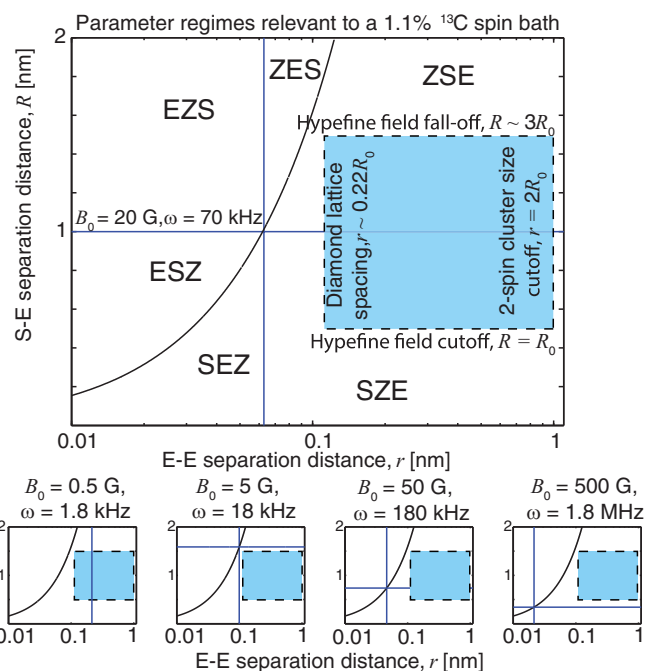


FIG. 6. (Color online) Plot showing the locations of the six parameter regimes in $R - r$ space for a naturally occurring 1.1% ^{13}C nuclear spin bath. The location of the intersection point (blue crosshairs) changes along the $S = E$ coupling line for different magnetic field strengths (the main plot depicts the case of 20 G, and the sequence below depicts the 0.5, 5, 50, and 500 G cases). For this spin bath, we see that only the regimes where $S \gg E$ (i.e., SEZ, SZE, and ZSE) are relevant.

that

$$0 \leq R \leq r \left(\frac{a}{b}\right)^{1/3}, \quad R \left(\frac{b}{a}\right)^{1/3} \leq r \leq \left(\frac{b}{\omega}\right)^{1/3}.$$

The remaining three regimes ZES, EZS, and ESZ may be quantified in an equivalent manner, however, the physical constraints placed on R and r due to the diamond lattice render these regimes impossible for a naturally occurring 1.1% ^{13}C nuclear spin bath. This is illustrated in Fig. 6, where the possible physical locations an environmental spin may occupy are shown in the shaded region. The constraints on r arise from the fact that no two spins may be within a distance of less than one lattice site from each other; whereas having a large separation means that there is little chance of the two spins in question being part of the same cluster (this will be quantified using the probability distributions for spin-spin separation distances discussed in Sec. IV). Similarly, the constraints on R arise from the lattice spacing, and the fact that the hyperfine field vanishes at large R . In particular, we see that, while changing the background field strength changes the relative number of spins in the ZSE, SZE, and SEZ regimes, a 1.1% ^{13}C nuclear spin bath will never occupy any regime for which $E \gg S$. That is, in solving for this particular physical system, we need not consider any of the ZES, EZS, or ESZ regimes.

This will not be true for all spin baths, however, as shown by Fig. 7, in which 1.1%, 0.3%, and 0.01% ^{13}C nuclear spin baths are considered, together with naturally occurring type-1b diamond containing an electron spin bath due to nitrogen donor

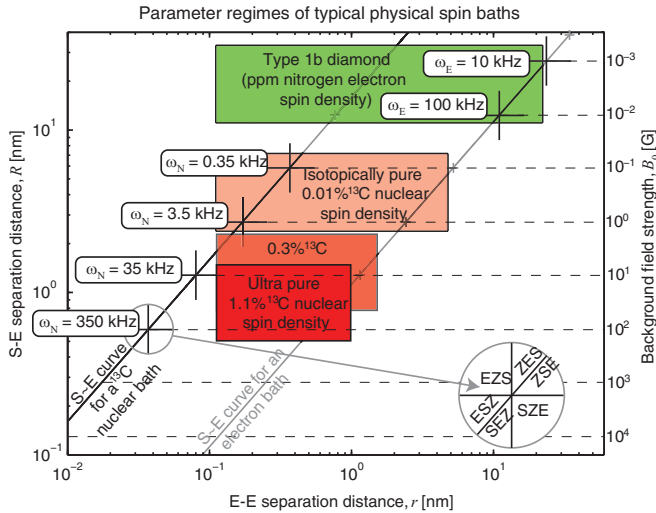


FIG. 7. (Color online) Plot showing the locations of the six parameter regimes in $R-r$ space for 1.1%, 0.3%, and 0.01% ^{13}C nuclear spin baths and a naturally occurring electron spin bath arising from nitrogen donor spins at ppm concentrations. For the latter example, we see that only the regimes where $E \gg S$ (i.e., ESZ, EZS, and ZES) are relevant.

impurities at parts-per-million (ppm) concentrations. The latter example presents a stark contrast to the 1.1% ^{13}C case, as the only appreciable regimes that need be considered here are ZES, EZS, or ESZ, a consequence of the comparatively strong electron-electron coupling of the environmental spins, however, electron spin baths are not the focus of this work.

In the present context, we define the decoherence of the NV as the loss of coherence between the $|0\rangle$ and $|+1\rangle$ states of the NV spin. This corresponds to the decay of the off-diagonal terms in the corresponding density matrix, and may be computed directly from the lateral (in the x - y plane) projection of the NV magnetization vector $L = \langle \mathcal{S}_x + i\mathcal{S}_y \rangle$. As the decoherence generally leads to a decay of this signal, we define a “decoherence function” $\Lambda(t)$, such that we may write $L = e^{-\Lambda(t)}$, and we refer to the time taken to reach $\Lambda(t) = 1$ as the “coherence time.” Our task is then to determine the functional form of Λ in response to the separate parameter regimes discussed above.

In order to determine the full decoherence behavior due to all spins in the environment, we may break up the environment into separate clusters consisting of strongly interacting spins and ignore the comparatively weak interactions between adjacent clusters. By virtue of the large zero-field splitting, and the maximum hyperfine coupling for an adjacent ^{13}C being of order 40 MHz, the NV spin exists in a “pure dephasing” regime in which only the relative phases of the spin states change and the respective populations do not. This will not be true for electron spin baths in the high-density limit, however, such systems are beyond the scope of this work. We may then write the Hamiltonian as $\mathcal{H} = \sum_k \mathcal{H}_k$, where \mathcal{H}_k acts only on the k th cluster. Since all of the \mathcal{H}_k ’s commute, the time-evolution operator may be factorized as $\mathcal{U}(t) = \prod_k \mathcal{U}_k(t)$. This implies that the full decoherence function is then simply a sum over all geometric configurations and locations of the environmental clusters. We note that this result will break down near the

anticrossing of the NV spin states at roughly 1024 G, as the nuclear spins will be able to exchange energy with the NV spin. However, as the linewidth of the spin bath is of order kHz, this effect corresponds to a very narrow magnetic field interval of roughly 0.1 G and is therefore ignored.

As we will show, incorporation of higher-order clustering has no effect on the leading-order behavior of the decoherence function, and is thus not important for the decoherence behavior in the presence of low-order pulse sequences such as free-induction decay (FID) and spin echo. In the following, we examine the decoherence functions associated with individual clusters of environmental spins, and then move on to discuss the statistics associated with how the environmental spins are distributed spatially. These distributions will then be used to compute the full decoherence behavior due to all clusters in the environment. In doing so, we consider two types of averaged quantities: the complete ensemble-averaged behavior of a large number of NV centers, each exposed to a separate realization of the environmental impurity distribution; and the “most likely” single realization of this distribution.

In light of the multitude of possible outcomes for the environmental spin distribution, and the large variation in the spin-echo behavior that results from this [12], we have chosen to place the majority of our focus on the ensemble-averaged behavior (i.e., as averaged over a large number of realizations of the environmental distribution), as is a standard approach for studies of this problem. Moreover, large ensembles of NV centers are fast becoming a common platform for sensing magnetic fields that are both weak in magnitude and complex in spatial variation [19,24,61], meaning a theoretical understanding of the ensemble’s collective behavior is necessary for its correct implementation. In this case, we regard every lattice site as having equal likelihood (1.1%) of being occupied by an impurity, and we average over all possible outcomes of the environmental distribution. In the case of a single realization, however, there will be a certain length scale surrounding the NV within which we do not expect to find any environmental spins, leading to a significant difference between the short-time behavior of the ensemble and that of a single realization of the environmental distribution. While the large variation in the possible realizations of this distribution make it difficult to account for every possible outcome, this approach allows us to investigate the short-time behavior of the system resulting from not having every site occupied. We note that the size of this void is essentially a free parameter, however, its properties may be quantified using the spatial statistics developed below. As we will see, this approach accurately accounts for the differences in behavior observed in experiments on ensemble and single-realization samples.

Owing to the lengthy quantitative development of the material presented in this work, we give an upfront discussion of the main results in the following section. The physics underpinning these results and the associated consequences are touched upon, however, all associated derivations and proofs are deferred until the relevant Appendix.

III. SUMMARY OF MAIN RESULTS

In this section, we give a summary of the main results of this work. This is done in the context of the three dynamic

processes taking place in the NV- ^{13}C composite system that are responsible for the decoherence of the NV spin. In each of these three cases, we begin by first considering isolated clusters of environmental spins, and then describe the effect of the environment as a whole, by summing the contributions from the individual clusters and averaging over all possible geometric configurations using the spatial statistics developed in Sec. IV. This allows us to rigorously determine both the time scales and exact analytic forms of the line shapes associated with each of the physical processes taking place in this system.

In the first instance, we examine the “natural” dynamics of the ^{13}C spin-spin environment (E-E) in the absence of the hyperfine field from the NV spin, and how these dynamics are influenced by their spatial distribution. We note that, despite the absence of the NV’s influence, this scenario is not as unrealistic as it may seem, as there is no effective hyperfine field when the NV spin is in its $|0\rangle$ state, meaning the environment is free to evolve as if the NV were not present. The autocorrelation (or spin-spin relaxation) times of the environment are found to be of the order of $T_c \approx 10$ ms, and are shown to be independent of the background magnetic field strength. This is in contrast to the analytic shape of the decay profile, which is shown to change dramatically over the range of field strengths considered. This is shown to be a consequence of whether the quantization axis of the environmental spins is set by their mutual coupling or by the external magnetic field. The details of this analysis may be found in Sec. V.

Having discussed the dynamic properties of the unperturbed spin-bath environment, the second and third cases are focused on the effect such an environment has on the coherence properties of a central NV spin. In the second case, we consider the effect of this hyperfine field (S-E) on the surrounding ^{13}C spins while ignoring the mutual spin-spin interactions examined in the previous case. Such an approximation is only valid for time scales that are much shorter than T_c , thus, we restrict ourselves to consideration of the FID, which occurs on time scales of $T_2^* \sim 1\text{--}10$ μs . From this analysis, we show that the FID of the central NV spin may be completely explained using an environment of ^{13}C spin that are uncoupled from one another. FID profiles are shown to exhibit a Gaussian-shaped decay for time scales less than that associated with the maximum hyperfine coupling in the system, followed by an abrupt transition to a linear-exponential decay. This leads to dramatic differences between profiles associated with an ensemble of NV spins and those due to single realizations of the environmental spin distribution. In the case of the former, the maximum possible hyperfine coupling is of the order of 100 MHz, meaning that the FID shows an exponential decay on all experimentally relevant time scales. On the other hand, in a typical realization of the environmental distribution, the nearest spin is likely to be more than a nanometer away, giving rise to hyperfine couplings of a few MHz or less. As such, FIDs of single NV spins typically exhibit a Gaussian shape. By increasing the strength of the external magnetic field, we may control whether the quantization axis of the environmental spins is set by the hyperfine coupling, or by the field itself. The transition from the former to the latter results in an increase in T_2^* by a factor of approximately 1.80 in the case of an

ensemble, and approximately 1.58 in the case of a typical single realization of the environmental distribution. The details of this analysis may be found in Sec. VI.

In the final case, having investigated both E-E and S-E processes separately, we move on to the analysis of the NV spin coherence in the presence of a spin-echo pulse sequence, as detailed in Sec. VII. This decoherence results from a combination of the E-E and S-E processes discussed above in what is essentially a two-stage process: entanglement between the NV spin and the surrounding spins is generated via the hyperfine interaction when the NV is in its $|+1\rangle$ state, however, the hyperfine field simultaneously prevents these spins from communicating with each other to any appreciable degree. Information about the NV that is encoded onto the environmental spins is therefore only able to propagate throughout the bath once the NV spin is pulsed into its $|0\rangle$ state and the hyperfine field is removed. Our results show that spin-echo coherence times may range from $T_2 \sim 100$ μs to $T_2 \sim 1$ ms, depending on the strength of the background field; a consequence of the transition from SEZ to SZE through to ZSE regimes. We initially consider scenarios in which the decoherence can be attributed to environments existing in each of these regimes exclusively, and then move on to consider the full dependence of the decoherence on the magnetic field strength.

The analytic shape of the spin-echo envelopes shows a complex time dependence. In all three regimes, an initially quartic exponential decay ($\Lambda \sim t^4$) is exhibited on free-precession time scales of $t < T_2^*$. In the purely SEZ regime, this transitions to a cubic dependence ($\Lambda \sim t^3$) for times $T_2^* < t \ll T_2$, whereas the SZE and ZSE regimes exhibit a ($\Lambda \sim t^{11/3}$) dependence on these time scales. Finally, as free-precession time scales approach the coherence time T_2 and beyond, all three regimes exhibit a Gaussian decay ($\Lambda \sim t^2$). It is the latter which is the most relevant to experiments conducted on NV centers coupled to a ^{13}C nuclear spin bath.

In analyzing the system’s response to a spin-echo pulse sequence, we also perform a detailed analysis of the periodic decays and revivals in the spin-echo envelope at moderate background magnetic field strengths. These revivals occur at half the Larmor frequency of the environmental spins, and are referred to as electron spin-echo envelope modulation (ESEEM). In addition to the revival frequency, both the depths of the decay valleys and the widths of the revival peaks show a very strong, nontrivial dependence on the background magnetic field strength. Specifically, we find that the depths to which these features decay scales as $|\Lambda_{\text{ZSE}}^{\text{ESEEM}}| \sim (354 \text{ G}/B_0)^2$ in the ZSE regime, meaning that the peaks do not decay completely in this regime (see Fig. 15). As the magnetic field is reduced to the SZE regime, not only do the peaks decay completely, their heights transition to a $|\Lambda_{\text{SZE}}^{\text{ESEEM}}| \sim 860 \text{ G}/B_0$ dependence on the background field strength. At high fields, the peak widths show a dependence of $T_{\text{W}}^{(\text{ZSE})} \sim 61 \mu\text{s G}^{1/2}/\sqrt{B_0}$, which transitions to $T_{\text{W}}^{(\text{SZE})} \sim 121 \mu\text{s G}^{2/3}/B_0^{2/3}$ in the SZE regime as was shown previously in the numerical work of Ref. [59]. In this work, we show that such behavior arises when considering time scales that are longer than that characterizing the hyperfine interaction ($t \sim T_2^*$), as is the case when ESEEM peak widths exceed T_2^*

TABLE I. Table summarizing the main results of this work. Note that consideration of the hyperfine field is not relevant to the discussion of the unperturbed nuclear-nuclear dynamics of the environment, meaning that ZSE and SZE effectively describe the same regime. Similarly, when discussing the purely hyperfine driven evolution of the environment, nuclear spin-spin couplings are not considered, meaning that SEZ and SZE describe the same regime.

Nuclear-nuclear dynamics	Low field (SEZ)	Moderate field (SZE)	High field (ZSE)
<i>Fundamental time scales</i>			
Maximum nuclear spin-spin coupling T_b	300 μ s		300 μ s
Correlation time of effective nuclear field T_c	10 ms		10 ms
<i>Autocorrelation function $\langle \mathcal{B}(t)\mathcal{B}(0) \rangle / \langle \mathcal{B}^2 \rangle$</i>			
Ensemble ($0 < t \lesssim T_b$)	$\sim 1 - (t/T_b)^2$		$\sim 1 - (t/T_b)^2$
Ensemble ($T_b \ll t \sim T_c$)	$\sim 1 - (t/T_c)$		$\sim 1 - (t/T_c)^{5/3}$
<i>NV-nuclear (hyperfine) dynamics</i>			
<i>Fundamental time scales</i>			
Maximum hyperfine coupling T_a		~ 10 ns	~ 10 ns
FID time T_2^* (ensemble)		1.63 μ s	2.92 μ s
FID time T_2^* (typical single realization)		3.53 μ s	5.58 μ s
<i>FID decoherence envelope L_{FID}</i>			
Ensemble		$\exp(-t/1.63 \mu\text{s})$	$\exp(-t/2.92 \mu\text{s})$
Typical single realization		$\exp[-(t/3.53 \mu\text{s})^2]$	$\exp[-(t/5.58 \mu\text{s})^2]$
<i>Combined dynamics</i>			
<i>Spin-echo decoherence</i>			
Coherence time, T_2	155 μ s	780 μ s	900 μ s
Envelope L_{SE} ($0 < t \ll T_2^*$)	$\exp[-(t/36 \mu\text{s})^4]$	$\exp[-(t/75 \mu\text{s})^4]$	$\exp[-(t/91 \mu\text{s})^4]$
Envelope L_{SE} ($T_2^* < t \ll T_2$)	$\exp[-(t/250 \mu\text{s})^3]$	$\exp[-(t/840 \mu\text{s})^{11/4}]$	$\exp[-(t/933 \mu\text{s})^{11/4}]$
Envelope L_{SE} ($t \sim T_2$)	$\exp[-(t/155 \mu\text{s})^2]$	$\exp[-(t/780 \mu\text{s})^2]$	$\exp[-(t/900 \mu\text{s})^2]$
<i>ESEEM</i>			
Revival period $2\pi/(\gamma_E B_0)$	N/A	1.8 ms G/ B_0	1.8 ms G/ B_0
Decay depth	N/A	$1 - \exp(-860 \text{ G}/B_0)$	$1 - \exp[-(354 \text{ G}/B_0)^2]$
Peak width T_w	N/A	121 μ s G $^{2/3}/B_0^{2/3}$	61 μ s G $^{1/2}/\sqrt{B_0}$

(below approximately 200 G), making short-time expansions of decoherence functions invalid.

Finally, we move on to discuss the validity of taking a semiclassical approach to modeling this system, in which the influence of the environment on the NV spin is replaced by an effective magnetic field whose dynamics may be inferred via consideration of the environmental interactions. We show that such an approach, when applied to a 1.1% ^{13}C nuclear spin bath, gives results that are in direct conflict with both experimental and numerical results, as well as the analytic results of this work. The reason for this stems from the hyperfine interaction being sufficiently large that its influence on the environmental spins cannot be ignored. As such, while the case of the native bath of P1 center electron spins remains unsolved, we note that the physical reasons leading to the failure of the semiclassical approach for the ^{13}C case are also directly applicable to the native electron spin bath of type-1b diamond. A detailed discussion of the above results is given in what follows.

IV. DISCUSSION OF RELEVANT DYNAMIC TIME SCALES

In this section, we discuss the spatial statistics associated with how spins in the environment arrange themselves with respect to one another. In the first instance, this gives us an indication of the expected time scales associated with

the system dynamics, however, these statistics will later be used to perform averages over the various possible geometric configurations of spin clusters in the environment, allowing us to derive collective autocorrelation and decoherence functions. An overview of these time scales is given in Table I.

In Appendix B, we find the probability distribution for the distance from a given spin in the bath to its k th nearest neighbor to be

$$P_k(r_k) = \frac{4\pi n r_k^2}{(k-1)!} \left(\frac{4\pi n r_k^3}{3} \right)^{k-1} \exp\left[-\frac{4\pi n r_k^3}{3}\right]. \quad (5)$$

This family of distributions will be used to determine the collective dynamic behavior of the environment and allow us to compare the contributions from the different orders of clustering.

Computing the mean distance to the k th neighbor, we find

$$\langle r_k \rangle = \left(\frac{4\pi n}{3} \right)^{-\frac{1}{3}} \frac{\Gamma(k + \frac{1}{3})}{(k-1)!}. \quad (6)$$

A plot of the time scales associated with the coupling of a given ^{13}C spin to its first 10 nearest neighbors versus their corresponding mean separation distances, $\langle r_k \rangle$ for $k = 1, \dots, 10$, is shown in Fig. 8. This relationship gives us an indication of how large the geometric size of a cluster may be (and hence the time scale) before next-nearest-neighbor (NNN) interactions become important. As we can see, for the

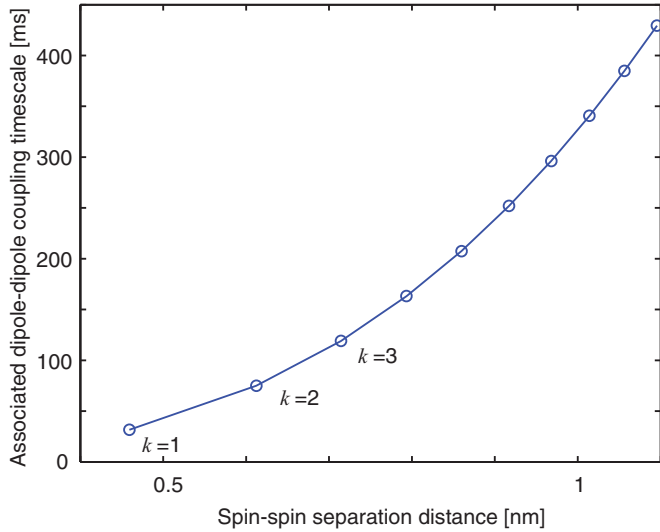


FIG. 8. (Color online) Plot of the time scales associated with the coupling of a given ^{13}C spin to its first 10 nearest neighbors vs their corresponding mean separation distance.

case of a NV center coupled to a ^{13}C nuclear spin bath, where $T_2 < 1$ ms, we need only consider two-spin interactions.

Time scales associated with the hyperfine interaction on the other hand, are much faster, with nuclear spins in adjacent lattice sites coupling to the NV spin with strengths of ~ 100 MHz. Given that such time scales are significantly shorter than the $T_2^* \sim 1\text{--}10$ μs and $T_2 \sim 1$ ms coherence times considered in this work (see Table I), the backaction of the NV spin on the environment is an effect that cannot be ignored, as is the case with semiclassical theories.

Having considered the approximate time scales of the physical processes taking place in this system, we now move on to describe the dynamical properties of these processes in detail.

V. ENVIRONMENTAL SPIN-SPIN (E-E) INTERACTIONS AND THE AUTOCORRELATION FUNCTION

Before deriving the decoherence functions associated with the FID and spin-echo evolution of the NV spin, we take a brief detour to examine the unperturbed dynamic behavior of the nuclear spin-bath environment. We do this by describing the effective semiclassical magnetic field felt at an arbitrary point in the lattice due to the interacting environmental spins. While the existence of such a field is not sufficient to describe the induced decoherence behavior of the central spin, due to the omission of the hyperfine influence, it does give us an insight into the natural dynamic behavior of the spin bath, and how it changes with the background magnetic field strength. In this section, we derive the autocorrelation functions of the effective magnetic field for both secular (high-field) and nonsecular (low-field) flip-flop regimes. We conclude this discussion of autocorrelation functions with an analysis of the effect of the hyperfine coupling on the nuclear spins, showing that its presence acts to suppress their flip-flop dynamics.

This analysis justifies why we may ignore the dipole-dipole coupling between nuclei when the NV spin is in either of the $|\pm 1\rangle$ states.

A. Secular dynamics ($Z \gg E$) of a single cluster

When a background field of sufficient strength to set the quantization axis of the spins in the cluster is applied, some of the terms in the Hamiltonian describe spin transitions that are no longer energy conserving and are hence disallowed (see Appendix A). The effective magnetic field operator as felt by the central spin is due to the axial components of the hyperfine interaction

$$\mathcal{B}_2 = \sum_{j=1}^{N_k} (A_{zx}^{(j)} \mathcal{E}_x^{(j)} + A_{zy}^{(j)} \mathcal{E}_y^{(j)} + A_{zz}^{(j)} \mathcal{E}_z^{(j)}), \quad (7)$$

where N_k is the number of spins in the k th cluster. In describing the purely axial dynamics of the nuclear spins, however, we need only consider the A_{zz} component (for the sake of brevity, the full description is omitted but may be found in Appendix A). For a two-spin cluster ($N_k = 2$), this leads to an autocorrelation function of

$$\langle \mathcal{B}_2(t) \mathcal{B}_2(0) \rangle_{ZE} = A_{z,1}^2 + A_{z,2}^2 - \Delta_z^2 \sin^2 \left(\frac{B_{12}t}{2} \right), \quad (8)$$

where $B_{12} = b/r_{12}^3 [1 - 3 \cos^2(\theta_{12})]$, and $\Delta_{x,y,z} \equiv |A_{x,y,z,1} - A_{x,y,z,2}|$. Since we are only concerned with couplings to the axial (z) component of the NV spin, we have adopted the shorthand notation of $A_{zz}^{(j)} \equiv A_{z,j}$.

Equation (8) shows that there is always a static component of the secular autocorrelation function present regardless of the geometric arrangement of the spins in the cluster. The total axial magnetization for a given cluster is constant, hence, the NV only sees a fluctuating field if the two spins have different hyperfine coupling strengths ($A_{z,1}$ and $A_{z,2}$). The larger this difference, the greater the strength of the effective fluctuating field, however, the axial flipping rate B_{12} decreases with their spatial separation. If the spins are sufficiently close together, such that their energy scale is dictated by their mutual interaction, non-energy-conserving transitions become permissible, and the secular condition is violated. This case is dealt with in Appendix A 1 b.

These methods may be extended to obtain corrections for three-spin interactions and higher. However, as will become clear later in this section, incorporation of high-order cluster sizes does not contribute to the leading behavior of the autocorrelation function (see Appendix A 1 a). Instead, these changes only become apparent on much longer time scales, as was alluded to in Sec. IV.

B. Nonsecular dynamics ($E \gg Z$) of a single cluster

In the opposite limit of low magnetic field strength, where the quantization axis of the nuclear spins is set by their mutual coupling, we cannot ignore the nonmagnetization conserving terms in the dipole tensor describing their interaction. The retention of all terms in the nuclear-nuclear dipole coupling tensor yields the following nonsecular autocorrelation function

of the axial magnetic field:

$$\langle \mathcal{B}_2(t)\mathcal{B}_2(0) \rangle_{\text{EZ}} = (A_{z1}^2 + A_{z2}^2) \left[1 - \frac{4}{3} \sin^2 \left(\frac{3B_{12}t}{4} \right) \right]. \quad (9)$$

Note that, where the secular autocorrelation function only had fluctuating components proportional to differences in probe-spin couple strengths (Δ_z) within a given cluster, the nonsecular function contains terms that are present regardless of the geometric arrangement of the cluster constituents. This is a consequence of the fact that, for a nonsecular cluster, the background field does not set the quantization axis of the spins, hence, the total magnetization component along the background field direction need not be constant. As we will see in Sec. V C, when the contributions to the full autocorrelation functions are summed over all clusters in the environment, we see very large differences between the dynamic behavior of spins in secular and nonsecular flip-flop regimes.

C. Collective environmental autocorrelation functions

Having just obtained the autocorrelation functions corresponding to the secular [Eq. (8)] and nonsecular [Eq. (9)] evolution of an individual cluster, we can employ the spatial statistics developed in the previous section to determine the respective autocorrelation functions due to the sum of all clusters in the environment. The explicit details of this derivation are given in Appendix C, and from this, we find the full autocorrelation function for a secular environment to be

$$\langle \mathcal{B}_2(t)\mathcal{B}_2(0) \rangle_{\text{ZE}} = \frac{8}{5} \left(\frac{4}{3} \pi a n \right)^2 \left[1 - \frac{1}{3} M(t) \right], \quad (10)$$

where $M(t)$ is related to the secular magnetization, as detailed in Appendix C, and is given to leading order in t by

$$M(t) \sim \frac{4\pi\sqrt[3]{6}}{\Gamma(\frac{8}{3})} (\pi b n t)^{5/3} - \frac{8\pi}{\sqrt{3}\Gamma(\frac{4}{3})} (\pi b n t)^2. \quad (11)$$

This gives an autocorrelation time of

$$T_{\text{ZE}} = \frac{9}{4\pi^2 b n} \approx 9.6 \text{ ms}. \quad (12)$$

On the other hand, the collective autocorrelation function for the nonsecular environment may be computed exactly,

$$\langle \mathcal{B}_2(t)\mathcal{B}_2(0) \rangle_{\text{EZ}} = \frac{64}{9} \pi^2 a^2 n^2 [1 - N(t)], \quad (13)$$

where $N(t)$ is related to the nonsecular magnetization, as detailed in Appendix C. To leading order, this results in a linear decay, given by

$$N(t) \sim \frac{4}{9} \pi^2 a^2 b n t, \quad (14)$$

and gives the same autocorrelation time of

$$T_{\text{EZ}} = \frac{9}{4\pi^2 b n} \approx 9.6 \text{ ms}. \quad (15)$$

While these regimes show an identical correlation time, the nonsecular regime shows a much greater fluctuation magnitude (see Fig. 9). This is a consequence of the fact that axial magnetization must be conserved for a cluster in a secular regime, meaning that the central spin can only sense an effective field fluctuation if there is a difference

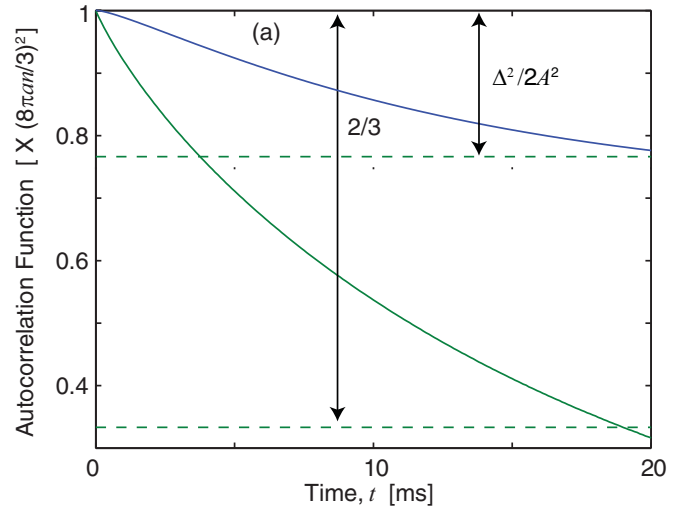


FIG. 9. (Color online) Normalized secular (blue) and nonsecular (green) autocorrelation functions.

in hyperfine couplings between the spins in that cluster. On the other hand, for the nonsecular case, it is the cluster geometry that sets their quantization axis, meaning that transitions that do not conserve axial magnetization are now allowed.

It is important to note that while these results hold on time scales of order $T_{\text{ZE,EZ}}$, they are not strictly correct for time scales associated with cluster sizes smaller than the diamond lattice spacing, i.e., $T_b \sim l^3/b \approx 300 \mu\text{s}$. The $M(t) \sim t^{5/3}$ scaling at ultrashort time scales is the result of the $p(r) \sim r^2$ scaling of the probability density function associated with the distance between neighboring spins, which breaks down on length scales of $r \sim l$. By expanding Eqs. (A9) and (A12) on time scales of order T_b , it is trivial to show the initial quadratic scaling of both secular and nonsecular autocorrelation functions.

A comparison of the collective autocorrelation functions associated with the secular and nonsecular regimes is plotted in Fig. 19(a), using $\langle A_z^2 \rangle = \frac{4}{5} \left(\frac{4\pi}{3} a n \right)^2$ and $\langle \Delta_z^2 \rangle \approx \frac{4}{5} (2a n)^2$ (the angular brackets denote a summation over all clusters, and an average over all possible arrangements of the spins within the cluster with respect to each other). From this, we see that not only is the magnitude of the decay much greater in the nonsecular case, but the nonsecular decay is purely linear at $t=0$, indicating a self-similar, Markovian regime at all time scales. On the other hand, the secular case has zero derivative at $t=0$, which is a consequence of the axial magnetization of the cluster being conserved due to the dominant Zeeman coupling of the cluster constituents.

D. Suppression of nuclear dynamics due to hyperfine fields

In cases where a strong magnetic field gradient exists, two nuclear spins will possess a mutual detuning between their respective Zeeman energies given by $\delta_z = |\omega_1 - \omega_2|$. As such, we expect that the magnitude of their effective magnetic field to be reduced. Solving for the autocorrelation function in this

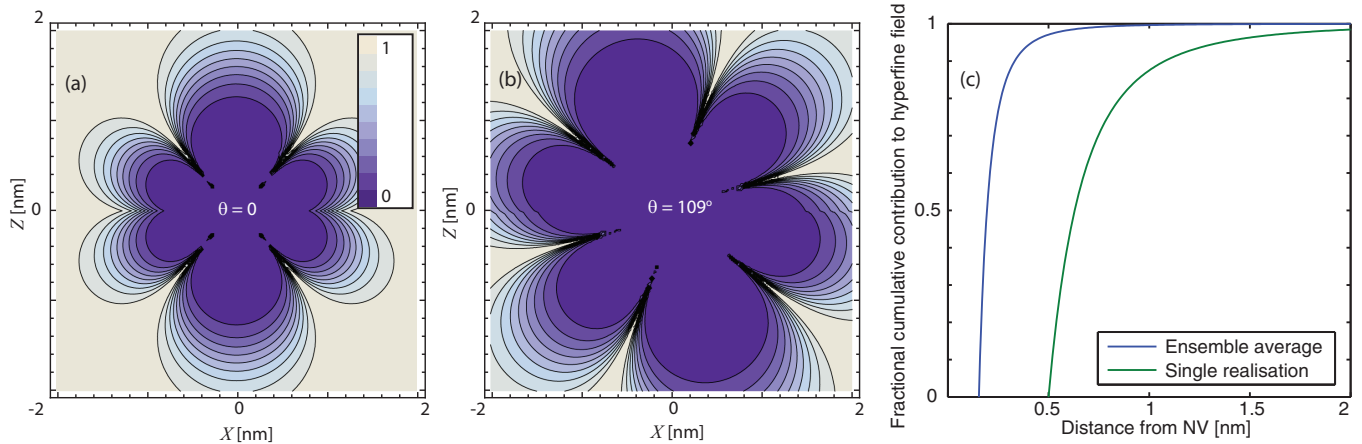


FIG. 10. (Color online) Plot showing the suppression of dipole-mediated nuclear spin dynamics due to the hyperfine field of the NV center. Values of the suppression constant K [see Eq. (17)] are plotted in (a) and (b) for cases where the two nuclei occupy adjacent lattice sites, with relative orientations of $\theta = 0^\circ$ and 109° , respectively. The fractional cumulative contribution of all nuclei within a distance R to the total hyperfine field is shown in (c) for both the ensemble case (blue) and that of a typical realization of the environmental spin distribution (green). This plot shows that effectively all nuclei making an appreciable contribution to the hyperfine field also reside in the suppression region.

case, we find

$$\langle B_2(t)B_2(0) \rangle = A_{z,1}^2 + A_{z,2}^2 - \Delta_z^2 \frac{B_{12}^2}{B_{12}^2 + \delta_z^2} \times \sin^2 \left(\frac{t}{2} \sqrt{B_{12}^2 + \delta_z^2} \right), \quad (16)$$

showing a modulation in the fluctuation amplitude by a factor of $B_{12}^2/(B_{12}^2 + \delta_z^2)$ as compared with Eq. (8), which becomes significantly damped as the magnitude of the detuning approaches that of the mutual dipolar coupling strength. We would not expect such a situation to arise as the result of inhomogeneities in an applied background as the associated detunings are simply not large enough over the distance of a few angstroms, which would require a magnetic field gradient of $\sim (b/l^3)/(l\gamma_E) \approx 1 \text{ mT nm}^{-1}$. Where significant detunings can arise, however, are as the result of the hyperfine field generated by the central NV spin. For nuclear spins up to a few nanometers from the NV center (which are responsible for the decoherence of the NV spin, as shown in Figs. 6 and 7), the difference in hyperfine couplings between two adjacent lattice sites is much greater than the associated dipolar coupling between them, leading to a complete suppression of the nuclear spin dynamics. We make this statement more precise as follows.

When the detuning between the Zeeman energies of two coupled nuclear spins is the result of the NV hyperfine field, we have that $\delta_z^2 = \Delta_z^2 = (A_{z,1} - A_{z,2})^2$. Equation (16) shows this leads to a suppression of the associated fluctuation amplitude by a factor of

$$K = \frac{B^2}{B^2 + \Delta_z^2}. \quad (17)$$

Consider the cluster arrangement depicted in Fig. 5. As the largest coupling strength comes from nuclei that occupy adjacent lattice sites, we take $r = l$, where $l = 1.54 \text{ \AA}$ is the lattice constant for diamond. From Eq. (3), the axial hyperfine

coupling strengths are given by

$$A_{z,i} = \frac{a}{R_i^3} [1 - 3 \cos^2(\Theta_i)], \quad (18)$$

and the nuclear dipolar coupling strength is

$$B = \frac{b}{j^3} [1 - 3 \cos^2(\theta)]. \quad (19)$$

Using these quantities, we plot the magnitude of the suppression constant K [Eq. (17)] in Fig. 10. These results depict the worst case scenario (where the dipolar coupling is maximal and the hyperfine detuning is minimal) for the two possible cluster orientations of $\theta = 0^\circ$ [Fig. 10(a)] and $\theta = 109^\circ$ [Fig. 10(b)], and show that the nuclear dynamics is still strongly suppressed for NV-nuclear separations greater than 1 nm, and as great as 2 nm in the $\theta = 109^\circ$ case.

Naturally, as the NV-nuclear separation distance increases, both the hyperfine field and the corresponding hyperfine field detuning between adjacent lattice sites will decrease. For large enough NV- ^{13}C separations, the dipolar coupling will eventually dominate over the hyperfine detuning, however, the reduced hyperfine coupling implies that spins in these regions will necessarily be too weakly coupled to the NV to have any effect on its evolution. To make this statement precise, consider the fractional contribution of the hyperfine field from a lower cutoff R_0 to an arbitrary radial distance R as given by

$$\int_{R_0}^R n A_z^2 d^3\mathbf{R} / \int_{R_0}^{\infty} n A_z^2 d^3\mathbf{R} = 1 - \frac{R_0^3}{R^3}, \quad (20)$$

where n is the average density of ^{13}C spin in the lattice. The choice of R_0 will depend on the diamond sample at hand. In an ensemble average over many environmental distributions, all lattice sites will be equally populated, meaning that we must choose $R_0 = l$ as our lower cutoff. On the other hand, in a single realization of the environmental distribution, we would not expect to find a nuclear spin within a distance of $R_0 = (3/4\pi n)^{1/3} = 0.5 \text{ nm}$, which we take as our lower cutoff. We plot Eq. (20) for these two cases in Fig. 10(c),

showing that there is effectively no contribution from spins residing more than a nanometer from the NV center. It is for this reason that nuclear-nuclear dipolar couplings may be ignored for cases where the NV spin state is in either of its $|\pm 1\rangle$ basis states. Furthermore, as the NV spin must be in either of these states to feel the effect of the dipole field, this shows that a semiclassical mean-field approach cannot reproduce the decoherence behavior of a NV center coupled to a nuclear spin bath. This will be explored further in Appendix E.

VI. NV-SPIN (S-E) INTERACTIONS AND THE FREE-INDUCTION DECAY

Having discussed the environmental dynamics of the nuclear spin flip flops as unperturbed by the presence of the central spin, we now discuss the exclusive hyperfine dynamics of environmental spins coupled to the NV without considering their mutual dipolar couplings. Again, this is not sufficient to explain the full decoherence behavior under spin-echo and higher-order pulse sequences, however, it does give us an insight into how the hyperfine dynamics transition from nonsecular to secular behavior with an increasing magnetic field strength. Furthermore, given that FID time scales are of the order of a few μs and thus too fast to see the effects of dipolar couplings between environmental spins, noninteracting spins are sufficient to explain all FID effects.

An experiment in which the central spin is left to evolve under the action of the environment alone is referred to as a free-induction decay (FID), and the majority of the associated dephasing may be attributed to inhomogeneous broadening from quasistatic components of the spin bath. In the case of a NV center in either an electron or a nuclear spin bath, this broadening is typically of the order of a few MHz, equating to an effective magnetic field of a few μT . As such, coherence times are typically of the order of $T_2^* \sim 1\text{--}10 \mu\text{s}$, depending on the sample at hand.

The exact FID decoherence function for an arbitrary magnetic field strength is given in Appendix A 2, Eq. (A14). Expanding this result for $\omega \gg A_z$, we find the contribution to the FID from a single spin to be

$$L_{\text{FID}}^{(1)}|_{\omega \gg A} \sim \cos\left(\frac{A_z t}{2}\right), \quad (21)$$

and in the low-field limit ($\omega \ll A_z$) we find

$$L_{\text{FID}}|_{\omega \ll A} \sim \cos\left(\frac{A t}{2}\right), \quad (22)$$

where $A = \sqrt{A_x^2 + A_y^2 + A_z^2}$.

There are a number of points worthy of discussion here, particularly with regard to the comparative strengths of the Zeeman and hyperfine couplings. In the infinite magnetic field limit, this coupling is completely determined by the axial hyperfine component A_z alone. This is because the Zeeman coupling is responsible for setting the quantization axis of the nuclei, hence, the NV spin is unable to drive transitions in the nuclear spins. On the other hand, in the zero-field case, it is the hyperfine coupling that sets the quantization axis of the nuclei, meaning that their magnetization need not be conserved with respect to the background magnetic field. This leads to a greater effective hyperfine coupling, owing to the inclusion

of A_x and A_y terms. This is an important effect that carries over into the analysis of higher-order pulse sequences, as it distinguishes the ZSE regime from the SZE and SEZ regimes.

We now consider the FID behavior of the NV spin due to the combined effect of all spin clusters in the environment. We first discuss the limiting regimes of both high and low magnetic fields as compared with the FID rate, and then move on to consider the full magnetic field dependence. We note that the time scales of the dipolar coupling in the environment are extremely slow (recall $T_S = T_N \sim 10 \text{ ms}$) compared to the $T_2^* = 1\text{--}10 \mu\text{s}$ FID times discussed here. This allows us to ignore the dipolar evolution, meaning that there are only two regimes important to the study of FID behavior, depending on the relative strengths of their Zeeman coupling (Z) to the background field, and their hyperfine coupling to the NV spin (S). Consequently, quantities derived in a regime where the Zeeman coupling dominates are labeled “ZS” and, similarly, quantities derived in a regime where the hyperfine coupling dominates are labeled “SZ.” While this is a somewhat simplistic situation compared with the six possible regimes discussed in Sec. II, these considerations detail the transition from secular to nonsecular hyperfine couplings with decreasing magnetic field, leading to faster decoherence, and are thus an important precursor to the spin-echo behavior to be discussed in Sec. VII.

Using Eq. (D3), the leading-order behavior of the FID decoherence functions in the ZS and SZ regimes [Eqs. (21) and (22)] is given by

$$\langle \Lambda_{\text{ZS}} \rangle \sim \left\langle 2 \sin^2 \left(\frac{A_z t}{4} \right) \right\rangle, \quad \langle \Lambda_{\text{SZ}} \rangle \sim \left\langle 2 \sin^2 \left(\frac{A t}{4} \right) \right\rangle, \quad (23)$$

respectively. Figure 11 shows the variation of the FID envelope with the strength of the axial background magnetic field B_0 , determined numerically, using a typical realization for the spin-bath distribution. From this, we see a monotonic increase of the FID time T_2^* , with increasing B_0 , which results in the transition of the effective hyperfine coupling strength from A to A_z , as detailed in Eqs. (21) and (22). For magnetic fields of $100 \text{ G} < B_0 < 1000 \text{ G}$, we observe what is essentially a hybrid regime, in which the decoherence envelope looks like that of the pure ZS and SZ regimes for times above and below the Larmor period $T_\omega \sim 2\pi/\gamma_E B_0$, respectively. This can be understood by recalling that spins in the SZ regime are those closest to the NV center ($R \lesssim a/\omega$), and are thus responsible for the short-time evolution of the NV spin. This contribution saturates beyond the Larmor period, however, from which point onward, where the remaining time evolution is governed by the weaker coupling to spins in the ZS regime.

A. FID at high magnetic fields (ZS)

For magnetic fields greater than $\sim 1000 \text{ G}$, every environmental spin will be in a regime where the Zeeman coupling is greater than the hyperfine coupling to the NV spin (SZ). To visualize the FID behavior in this regime, we first employ a numerical cluster expansion method (to zeroth order, since nuclear-nuclear interactions are not important), from which an ensemble average is performed over some 10^6 realizations of the environmental spin distribution. The resulting ensemble-averaged decoherence function $\langle \Lambda_{\text{ZS}} \rangle$ is

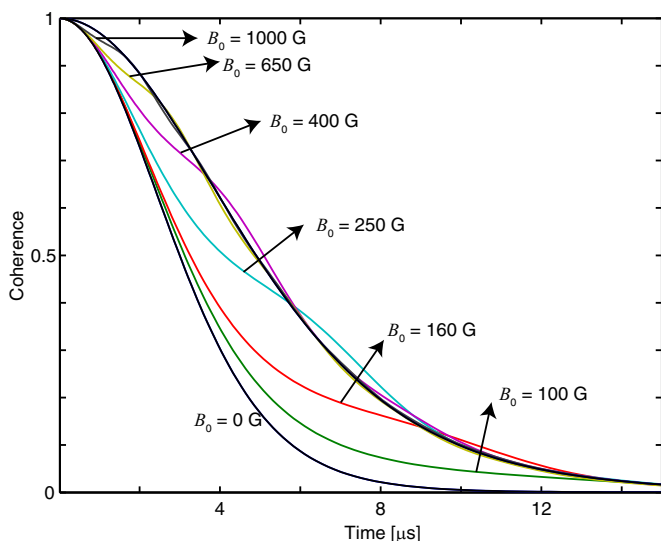


FIG. 11. (Color online) Plot showing the variation of the FID envelope with the strength of the background magnetic field. The transition from a SZ to a ZS regime occurs in the range of $100 \text{ G} < B_0 < 1000 \text{ G}$ at times associated with the Larmor period $T_\omega \sim 2\pi/\gamma_E B_0$.

plotted in Fig. 12(a). From this, we can see a linear scaling of the decoherence function for times approaching the FID time T_2^* (where $\langle \Lambda_{ZS} \rangle \sim 1$) and beyond, however, a quadratic scaling is shown for times much shorter than this. Furthermore, the quadratic scaling is shown to persist for much longer in the case of individual realizations than for the ensemble-averaged function. The analytic origins of these features are discussed in what follows.

To obtain the ensemble-averaged behavior, we must integrate over all possible outcomes of the environmental impurity distribution, which means that all lattice sites will be populated

with equal likelihood. The long-time behavior arises from the low-frequency ($\sim 1/T_2^*$) contributions to $\langle \Lambda_{ZS} \rangle$, corresponding to spins more than a few lattice sites (roughly a nanometer) away from the NV, where the distribution effectively constitutes a continuum. The short-time behavior, however, arises from spins that occupy the lattice sites surrounding the NV, where the bond length of the diamond lattice l is important, i.e., on time scales of $T_a = l^3/a \approx 50 \text{ ns}$. These features may be reproduced by integrating Λ_{ZS} over R from the diamond bond length l to ∞ , and over Θ from 0 to π (see Appendix D 1 for details). In the long-time limit, where $t \gg t_a$, we find

$$\langle \Lambda_{ZS} \rangle|_{t \sim T_2^*} = \frac{4\pi^2}{9\sqrt{3}} ant, \quad (24)$$

showing a linear exponential free-induction decay

$$\langle L_{ZS} \rangle = \exp\left(-\frac{t}{T_2^*}\right), \quad (25)$$

where the free-induction decay time is $T_2^* = \frac{9\sqrt{3}}{4\pi^2 an} = 2.92 \mu\text{s}$. For times shorter than T_a , we find a quadratic scaling in the decoherence function, given by

$$\langle \Lambda_{ZS} \rangle|_{0 < t \ll T_2^*} \sim \frac{2\pi a^2 n t^2}{15l^3} = \left(\frac{t}{960 \text{ ns}}\right)^2. \quad (26)$$

Both the long- and short-time analytic scalings are plotted together with the numerical results in Fig. 12(a), showing excellent agreement.

While this analysis accurately reproduces the experimental results for FID experiments conducted on NV ensembles (see, for example, Ref. [62]), experiments conducted on single NV centers exhibit a Gaussian-shaped decay that typically persists as long as T_2^* . To reproduce this behavior, we instead integrate $\langle \Lambda_{ZS} \rangle$ from R_0 to ∞ , as we would expect to find less than one impurity within a radius of R_0 from the NV center. Following the same steps as in the ensemble case above, we find an initial

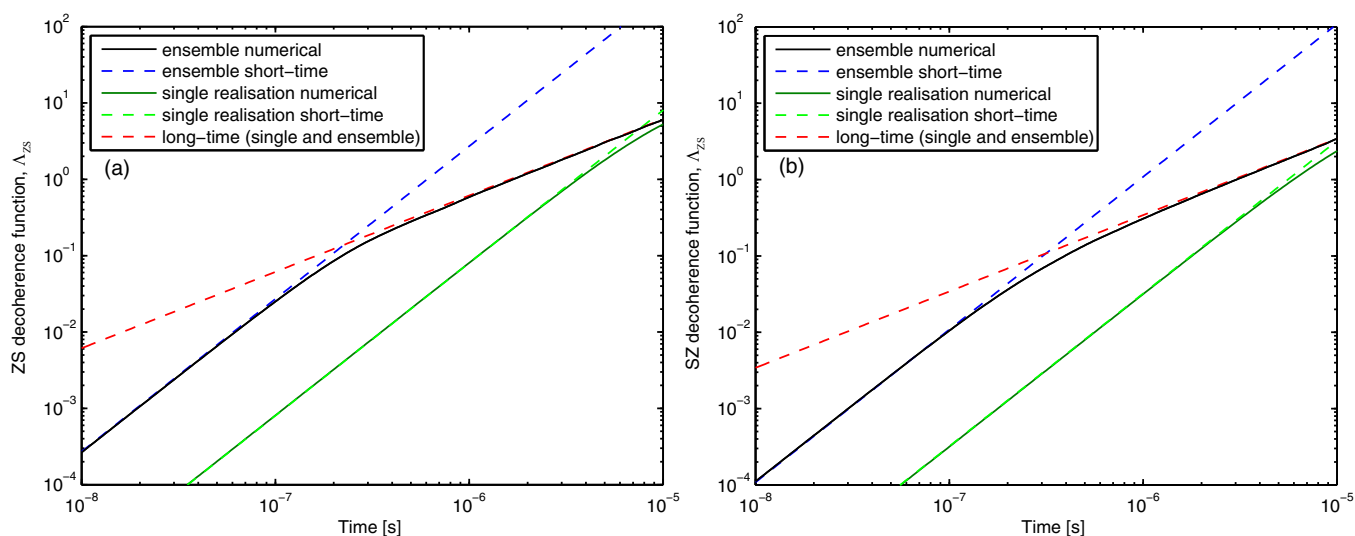


FIG. 12. (Color online) (a) Plot showing the behavior of the FID decoherence function in the high-field (ZS) regime $\langle \Lambda_{ZS} \rangle$. The solid black curve shows the numerical calculation over 10^6 realizations of the nuclear spin distribution, and the blue and red dashed curves depict the short/quadratic and long/linear analytic limits (see main text). The solid green curve shows the behavior of a single realization of the nuclear spin distribution, with the green dashed line showing the quadratic short-time behavior, that persists for times beyond T_2^* . The long-time limit of the single realization behavior is identical to that of the ensemble case. (b) As in (a), but for the low-field (SZ) regime.

quadratic scaling of

$$\langle \Lambda_{ZS} \rangle |_{t \sim T_2^*}^{(\text{single})} = \frac{8}{45} \pi^2 a^2 n^2 t^2 = \left(\frac{t}{5.58 \mu\text{s}} \right)^2, \quad (27)$$

followed by the same linear scaling as detailed in Eq. (24). The crossover point of these two regimes occurs at $t = 5/[2\sqrt{3}an] \approx 11 \mu\text{s}$, which is well past the point at which decoherence has occurred, showing that the FID behavior of a single NV center spin is dominated by a Gaussian decay.

B. FID at low magnetic fields (SZ)

Following on from the high-field limit of the previous section, we now move on to discussing the FID behavior in the low-field limit, the numerical result for which is shown in Fig. 12(b). This analysis is performed in an identical manner, save for the replacement of $A_z \mapsto A$, as dictated by Eq. (23). This leads to a slight increase in the FID rate but qualitatively identical behavior as the ZS regime. For the long-time limit, we obtain

$$\langle \Lambda_{SZ} \rangle |_{t \sim T_2^*} = \frac{\pi^2}{18} [6 + \sqrt{3} \operatorname{arcosh}(2)] ant, \quad (28)$$

again showing a linear exponential free-induction decay, where the free-induction decay time is now $T_2^* = 18/[\pi^2 an [6 + \sqrt{3} \cosh^{-1}(2)]] = 1.63 \mu\text{s}$. For times shorter than t_a , we again see a quadratic scaling in the decoherence function, given by

$$\langle \Lambda_{SZ} \rangle |_{0 < t \ll T_2^*} \sim \frac{\pi a^2 n t^2}{3l^3} = \left(\frac{t}{607 \text{ ns}} \right)^2. \quad (29)$$

Finally, for the case of a typical single realization of the SZ spin-bath distribution, we find

$$\langle \Lambda_{SZ} \rangle |_{t \sim T_2^*}^{(\text{single})} = \frac{4}{9} \pi^2 a^2 n^2 t^2 = \left(\frac{t}{3.53 \mu\text{s}} \right)^2. \quad (30)$$

Both the long- and short-time analytic scalings are plotted together with the numerical results in Fig. 12(b), showing excellent agreement.

It is interesting to note that in the single-realization case, taking the ratio of the FID times for the high- and low-field cases gives

$$\frac{T_{2,ZS}^*}{T_{2,SZ}^*} = \sqrt{\frac{5}{2}} \approx 1.58, \quad (31)$$

in agreement with both the theoretical and experimental results of Ref. [63], whereas for the ensemble case we have

$$\frac{T_{2,ZS}^*}{T_{2,SZ}^*} = \frac{3}{8} [2\sqrt{3} + \cosh^{-1}(2)] \approx 1.80, \quad (32)$$

showing the ensemble FID times experience a greater enhancement from an increased magnetic field strength than those of a single realization of the bath impurity distribution.

VII. COMBINED HYPERFINE AND DIPOLAR INTERACTIONS, AND SPIN-ECHO DECAY

The relatively short coherence times of a FID experiment may be extended by 2–4 orders of magnitude by applying an

appropriate sequence of π pulses (or “bit-flips”), under which the quantum amplitudes of the $|1\rangle$ and $|0\rangle$ states are swapped. In the simplest instance, we consider a Hahn-echo or spin-echo pulse sequence, involving a single π pulse applied at time $t/2$ (halfway through the free-precession time t). The effect of this sequence is to refocus any static components of the bath, thereby extending coherence times by roughly 2 orders of magnitude, with typical times of 400 μs –1 ms.

It is important to note that, due to the secular approximation imposed on the NV center, this dominant S-E interaction is only apparent when the NV spin is in the $|+1\rangle$ state. In this case, the large hyperfine interaction results in the nuclei having a large mismatch in their respective transition frequencies, meaning their comparatively weak mutual dipole interaction will be unable to cause a mutual flip flop (this effect is discussed in Sec. VD). This is somewhat advantageous, as the exponentiation of the full Hamiltonian, inclusive of all \mathcal{H}_{SE} , \mathcal{H}_{ZE} , and \mathcal{H}_{EE} terms, is not analytically possible in general. On the other hand, when the NV spin is in the $|0\rangle$ state, there will be no hyperfine coupling, and the environmental evolution will be self-governed. This means that the environmental spins are free to evolve unperturbed according to \mathcal{H}_{ZE} and \mathcal{H}_{EE} .

In the previous sections, we discussed how treating the dipolar-dipole coupled nuclear spin bath as a fluctuating magnetic field does not explain the decoherence of the NV spin, as the NV can only sense the effect of the nuclei if its hyperfine field is simultaneously suppressing their activity. On the other hand, treatment of the hyperfine interaction exclusively, to the exclusion of the nuclear dipolar interaction, only shows periodic entanglement between the NV spin and the nuclei, with no permanent decay of NV spin coherence on long time scales [see Appendix A2, Eq. (A15)]. These results imply that the NV spin coherence is essentially a two-part process (see Fig. 3), in which quantum information of the NV spin is first imparted to the independent nuclei via the hyperfine interaction when the NV spin is in the $|+1\rangle$ state. This information may then be propagated throughout the crystal via the nuclear dipole-dipole interaction, while the NV spin is in the $|0\rangle$ state. As such, we must incorporate both interactions in order to be able to analyze the true decoherence behavior of the NV spin.

From Appendix A3, the leading-order behaviors of the decoherence functions for the ZSE, SZE, and SEZ regimes are given by

$$\begin{aligned} \langle \Lambda_{ZSE} \rangle &\sim \left\langle \sin^2 \left(\frac{Bt}{4} \right) \sin^2 \left(\frac{\Delta_z t}{4} \right) \right\rangle, \\ \langle \Lambda_{SZE} \rangle &\sim \left\langle \sin^2 \left(\frac{Bt}{4} \right) \sin^2 \left(\frac{\Delta t}{4} \right) \right\rangle, \\ \langle \Lambda_{SEZ} \rangle &\sim \left\langle \frac{8}{15} \sin^2 \left(\frac{3Bt}{4} \right) \left[\sin^2 \left(\frac{At}{2} \right) + \sin^2 \left(\frac{At}{4} \right) \right] \right\rangle, \end{aligned} \quad (33)$$

respectively.

The changes in behavior of the decoherence function Λ as we move from high- to low-field mirror what we have already observed when considering the environmental dipole-dipole coupling and NV-environment hyperfine processes exclusively. In the high-field (ZSE) case, the effect of the environment is ultimately determined by the difference in

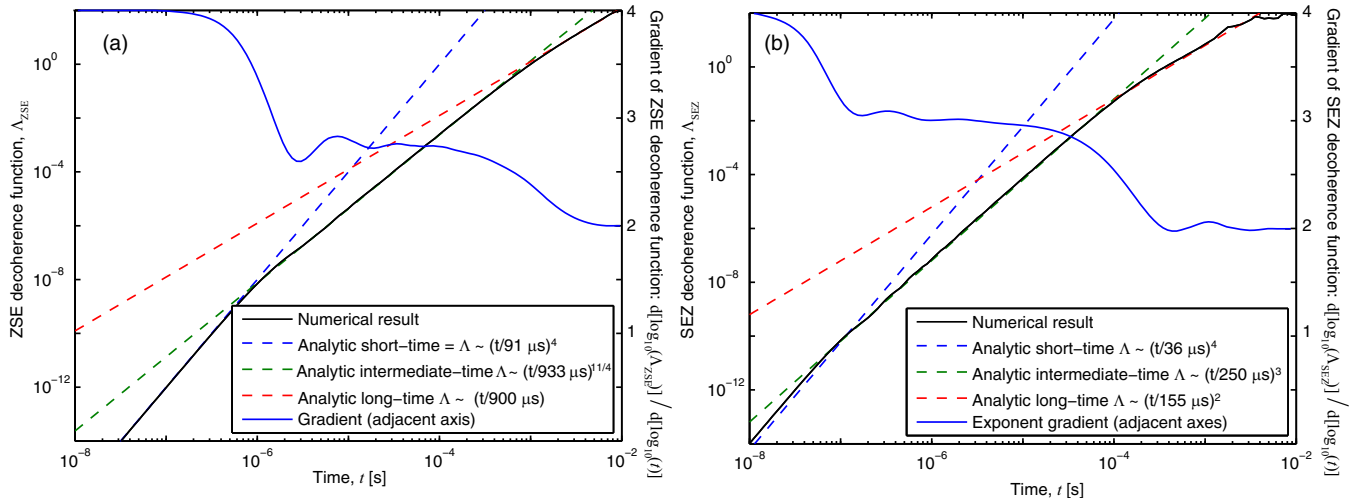


FIG. 13. (Color online) Plot showing the agreement between numerical and analytic results for the decoherence of a NV center spin in a 1.1% ^{13}C nuclear spin bath. (a) Results for the ZSE regime. The black curve shows the numerical result for $\langle \Lambda_{\text{ZSE}} \rangle$ computed using a seventh-order cluster expansion method (with cluster sizes of up to seven spins) averaged over 10^6 realizations of the surrounding impurity distribution. Analytic results for the short-, intermediate-, and long-time scalings are given by the blue, green, and red dashed curves, respectively. The scaling exponent, found by numerically computing $k = d[\ln(\langle \Lambda_{\text{ZSE}} \rangle)]/d[\ln(t)]$ is plotted as the blue solid curve (adjacent axis), and shows the transition from 4 to 2.75 to 2, as consistent with the analytic results. (b) As in (a) but for the SEZ regime.

axial hyperfine couplings between the spins in the cluster (Δ_z), and is further modulated due to the interactions taking place amongst these spins. As the field is decreased to the SEZ regime, the hyperfine interaction becomes dominant and all hyperfine components coupling to S_z become relevant, as was observed in the FID case above. Finally, as the magnetic field is decreased below the coupling between adjacent nuclear spins, their combined axial magnetization is no longer a conserved quantity, and the effect transitions from a difference in hyperfine couplings Δ to the full interaction A . This is the same as was observed in the autocorrelation function of the effective environmental magnetic field over the transition between secular and nonsecular regimes.

A. Spin-echo decay at high magnetic fields (ZSE)

At magnetic fields in excess of a few hundred Gauss, every ^{13}C nuclear spin exists in the ZSE regime. Thus, to compute the ensemble-averaged decoherence function for the high-field case, we integrate Λ_{ZSE} over the spatial distributions of the environmental spins (as detailed in Appendix D 2 a). A numerical calculation using the cluster expansion method (with cluster sizes up to seven spins) over 10^6 realizations of the impurity distribution is shown in Fig. 13(a), from which we see a number of complex features. In particular, the scaling of Λ_{ZSE} with t changes significantly between $t = 0.1$ and 1 ms from $\Lambda_{\text{ZSE}} \sim \mathcal{O}(t^{2.75})$ to $\Lambda_{\text{ZSE}} \sim \mathcal{O}(t^2)$. At very short times, where $t \ll T_2^*$, we find $\Lambda_{\text{ZSE}} \sim \mathcal{O}(t^4)$. The analytic origins of these scalings are discussed in what follows.

We initially consider the long-time limit, where the decoherence function exhibits a quadratic scaling (equivalently, the decoherence envelope exhibits a Gaussian decay). Such time scales are still much shorter than the environmental correlation time, however, meaning that we may expand Δ_z for small r , giving $\Delta_z \sim \frac{a_\alpha r}{R^4}$. Integration of Λ_{ZSE} over $0 \leq r, R \leq \infty$

yields (see Appendix D 2 a for details)

$$\langle \Lambda_{\text{ZSE}} \rangle|_{t \sim T_2} \sim \pi (ant)^{3/4} (bnt)^{5/4}, \quad (34)$$

giving a spin-echo coherence time of

$$T_2^{\text{ZSE}} = [\pi (an)^{3/4} (bn)^{5/4}]^{-1/2} = 900 \mu\text{s}, \quad (35)$$

in excellent agreement with the numerical results of Ref. [59].

Prior to this quadratic scaling, Λ_{ZSE} exhibits a scaling of $\sim \mathcal{O}(t^{11/4})$, which, as we detail below, is the result of spin impurities only being able to adopt discrete positions within the lattice. Such effects become important at short time scales, where the correspondingly small separation distances begin to approach the atomic spacing in the crystal. We can reproduce the effect of this spacing by choosing a lower cutoff for r of the diamond bond length $l = 1.54 \text{ \AA}$ (see Appendix D 2 a for details), giving

$$\langle \Lambda_{\text{ZSE}} \rangle|_{T_2^* < t \ll T_2} \sim \frac{a^{3/4} b^2 n^2 t^{11/4}}{l^{9/4}} = \left(\frac{t}{933 \mu\text{s}} \right)^{11/4}. \quad (36)$$

This expression shows perfect agreement with the numerical calculation in terms of both scaling and magnitude, as depicted in Fig. 13. At longer time scales, the magnitude of $\langle \Lambda_{\text{ZSE}} \rangle$ becomes much larger than the discrete correction term, and we simply recover the expression given in Eq. (35). This is to be expected: at long time scales, dipole-dipole interactions from spin impurities occupying adjacent sites essentially average out due to their high-frequency behavior, whereas the more long-range interactions become important. As the separation distance increases, the number of sites available for occupation essentially approaches that of a continuum.

Finally, to deduce the short-time quartic scaling, we again integrate over R and r from l to ∞ , and compute the formal short-time expansion, valid for $t: at/l^3 \ll 1$ and $bt/l^3 \ll 1$. As the smallest possible separation distance is l , we are only justified in making this expansion for $t < 50$ ns in the

ensemble case. The resulting expression is, to leading order (see Appendix D 2 a for details),

$$\begin{aligned} \langle \Lambda_{\text{ZSE}} \rangle|_{t \ll T_2^*} &= \frac{1}{80} \left(\frac{\pi n a b t^2}{l^3} \right)^2 \left[1 - \frac{\sqrt[6]{3} \pi l (4\pi n)^{1/3}}{360 \Gamma(\frac{4}{3})} \right] \\ &= \left(\frac{t}{91 \mu\text{s}} \right)^4. \end{aligned} \quad (37)$$

We note that some variation will exist between individual realizations of the impurity distribution, as most NV centers will not have spin impurities on adjacent lattice sites, meaning that the quartic scaling may persist for longer than in the ensemble case. To show this, we instead perform the R integral from a lower cutoff $R_0 = [3/(4\pi n)]^{(1/3)}$, defining the radius of a spherical volume in which we would expect to find less than one impurity on average for the ensemble case, meaning we would not expect impurities at distances closer than this in most individual cases. On the other hand, even the case of an individual distribution involves the NV coupling to many clusters, hence, there is a large enough sampling of possible cluster configurations to justify an average over these configurations. Integrating $\langle \Lambda_{\text{ZSE}} \rangle$ over R from R_0 to ∞ , and over r from l to ∞ , we find

$$\begin{aligned} \langle \Lambda_{\text{ZSE}} \rangle|_{t \ll T_2^*}^{(\text{single})} &= \frac{1}{90} \pi^4 a^2 b^2 n^4 t^4 \left(\frac{\sqrt[3]{6}}{l(\pi n)^{1/3}} - \frac{4\sqrt{3}\pi}{9\Gamma(\frac{4}{3})} \right) \\ &= \left(\frac{t}{393 \mu\text{s}} \right)^4, \end{aligned} \quad (38)$$

again showing a quartic scaling of $\langle \Lambda_{\text{ZSE}} \rangle$ with t , but one that persists for some 10–100 μs , as opposed to the 50 ns for the ensemble case.

B. Spin-echo decay at moderate magnetic fields (SZE)

At magnetic fields between 0.01 and 100 G, every ^{13}C nuclear spin exists in the SZE regime. The procedure to compute the ensemble-averaged decoherence function is the same as for that above, however, we simply make the substitution $\Delta_z \mapsto \Delta$ (see Appendix D 2 b for details). All subsequent results scale accordingly, the most important of which is $T_2^{\text{SZE}} = 780 \mu\text{s}$. Other notable properties that emerge in this regime are the electron spin-echo envelope modulation (ESEEM) peaks, which manifest as periodic decays and revivals at half the Larmor frequency of the NV. As these effects do not represent any true decoherence, we defer their discussion until Sec. VII E.

C. Spin-echo decay at low magnetic fields (SEZ)

At magnetic fields below 0.01 G, every ^{13}C nuclear spin exists in the SEZ regime. The transition of the fluctuation amplitude from Δ to A effectively decouples the S-E from the E-E evolution in Λ_{SEZ} , drastically changing the nature of the resulting decoherence. This allows for a convenient separation of the contribution of the hyperfine and dipolar coupling to the overall decoherence. A calculation of the decoherence function using a numerical cluster expansion to seventh order is shown in Fig. 13(b) for 10^6 realizations of the impurity distribution, from which a number of features are evident. As with the

ZSE and SZE regimes, we see quartic and quadratic scalings at short and long times, respectively, but in contrast to the other regimes, we see a cubic scaling at intermediate times. Furthermore, the coherence times exhibited by the SEZ regime are effectively an order of magnitude shorter than the other two regimes. The analytic origins of these features are explained in what follows.

As with the ZSE and SZE cases, we begin with the consideration of the long-time dynamics of the SEZ regime. As before, we need not worry about the discretized lattice at these time scales, and we therefore integrate Λ_{SEZ} over both R and r from 0 to ∞ (see Appendix D 2 c for details), giving

$$\langle \Lambda_{\text{SEZ}} \rangle|_{t \sim T_2} \sim \frac{2}{15} a b (\pi^2 n t)^2 = \left(\frac{t}{155 \mu\text{s}} \right)^2. \quad (39)$$

Again, we see an overall Gaussian behavior at long time scales, but a very different dependence on the hyperfine and dipolar dynamics of the environment ($\Gamma_{\text{ZSE,SZE}} \sim a^{3/4} b^{5/4}$ versus $\Gamma_{\text{SEZ}} \sim a b$). This is a consequence of the changes in behavior of the environmental autocorrelation function as the environment transitions from secular to nonsecular dynamics. The corresponding coherence time of the SEZ regime is $T_2^{\text{SEZ}} = 155 \mu\text{s}$.

To derive the intermediate cubic scaling of $\langle \Lambda_{\text{SEZ}} \rangle$, we note that, as was the case with $\langle \Lambda_{\text{ZSE}} \rangle$ and $\langle \Lambda_{\text{SZE}} \rangle$, the integral of $\sin^2(\frac{3Bt}{4})$ over the cluster size distribution [Eq. (B3)] from l to ∞ has no closed form. As such, we simply expand $P(r)$ for small r , as detailed in Appendix D 2 c, giving

$$\begin{aligned} \langle \Lambda_{\text{SEZ}} \rangle|_{T_2^* < t \ll T_2} &\sim \frac{\pi^3 a b^2 n^2 t^3 [2(4\gamma - 5)\pi l^3 n + 3]}{15 l^3} \\ &= \left(\frac{t}{250 \mu\text{s}} \right)^3. \end{aligned} \quad (40)$$

To determine the short-time scaling, we again integrate Λ_{SEZ} over R and r from l to ∞ , and use the same short-time expansion as employed in the ZSE case. As the smallest possible separation distance is l , we are only justified in making this expansion for $t < 50$ ns in the ensemble case. The resulting expression has (see Appendix D 2 c for details) an initially quartic dependence on time given by

$$\begin{aligned} \langle \Lambda_{\text{SEZ}} \rangle|_{t < T_2^*} &\sim \frac{5}{48} \left(\frac{\pi a b n t^2}{l^3} \right)^2 [2(4\gamma - 5)\pi l^3 n + 3] \\ &= \left(\frac{t}{36 \mu\text{s}} \right)^4, \end{aligned} \quad (41)$$

where $\gamma \approx 0.577$ is the Euler-Mascheroni constant.

D. Full magnetic field dependence

We now consider the full magnetic field dependence of the coherence time of a NV center exposed to a 1.1% ^{13}C nuclear spin bath. The full spin-echo envelope is the product of contributions from the six parameter regimes, with the dominant contribution coming from the ZSE, SZE, and SEZ regimes, $S_{\text{C13}} \approx S_{\text{ZSE}} S_{\text{SZE}} S_{\text{SEZ}}$, which implies the full decoherence function is given by the sum of decoherence functions due to each region,

$$\langle \Lambda_{\text{C13}} \rangle = \langle \Lambda_{\text{ZSE}} \rangle_{r > r_Z}^{R > R_Z} + \langle \Lambda_{\text{SZE}} \rangle_{r > r_Z}^{R < R_Z} + \langle \Lambda_{\text{SEZ}} \rangle_{r < r_Z}^{R < R_Z},$$

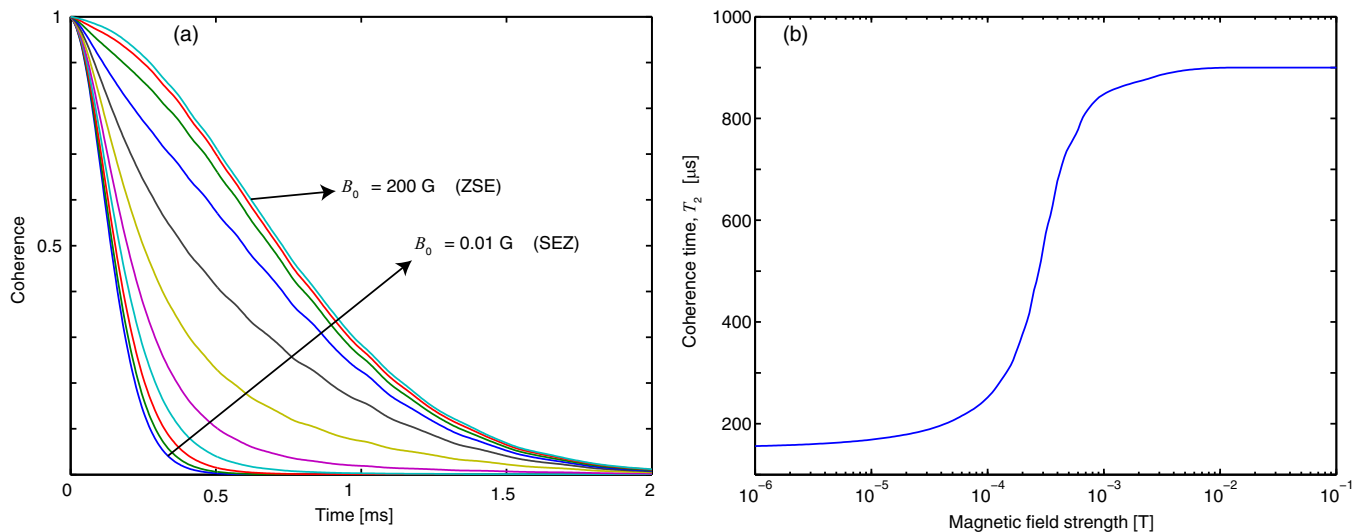


FIG. 14. (Color online) Magnetic field dependence of the NV spin coherence. (a) Coherence envelopes of a NV center coupled to a naturally occurring 1.1% ¹³C nuclear spin bath corresponding to external magnetic field strengths from 10 μT to 10 mT. (b) Plot showing the dependence of the coherence time on the strength of an external magnetic field.

where the R_z and r_z quantities denote the Zeeman-dependent integration domains in $r - R$ space.

Figure 14(a) shows gradual transition of the decoherence envelopes from the SEZ regime through to the ZSE regime with increasing magnetic field. The full dependence of the corresponding coherence times T_2 is shown in Fig. 14(b), where we see that coherence times of a NV spin coupled to the naturally occurring 1.1% ¹³C nuclear spin bath can be almost 1 ms for magnetic fields in excess of 100 G. Our results show excellent agreement with the extensive numerical

investigation conducted in Ref. [59]. The persistent Gaussian shape predicted by our theory is a radical departure from currently accepted theories in the literature claiming either a $\Lambda \sim (t/T_2)^3$ and $\Lambda \sim (t/T_2)^4$ dependence irrespective of the physical origin of the spin bath. We have shown here that the former is not valid for the case of a NV center immersed in a ¹³C nuclear spin bath, except where spin densities are well below those currently realized experimentally. The latter is only valid in the short-time limit, and may be explained as follows.

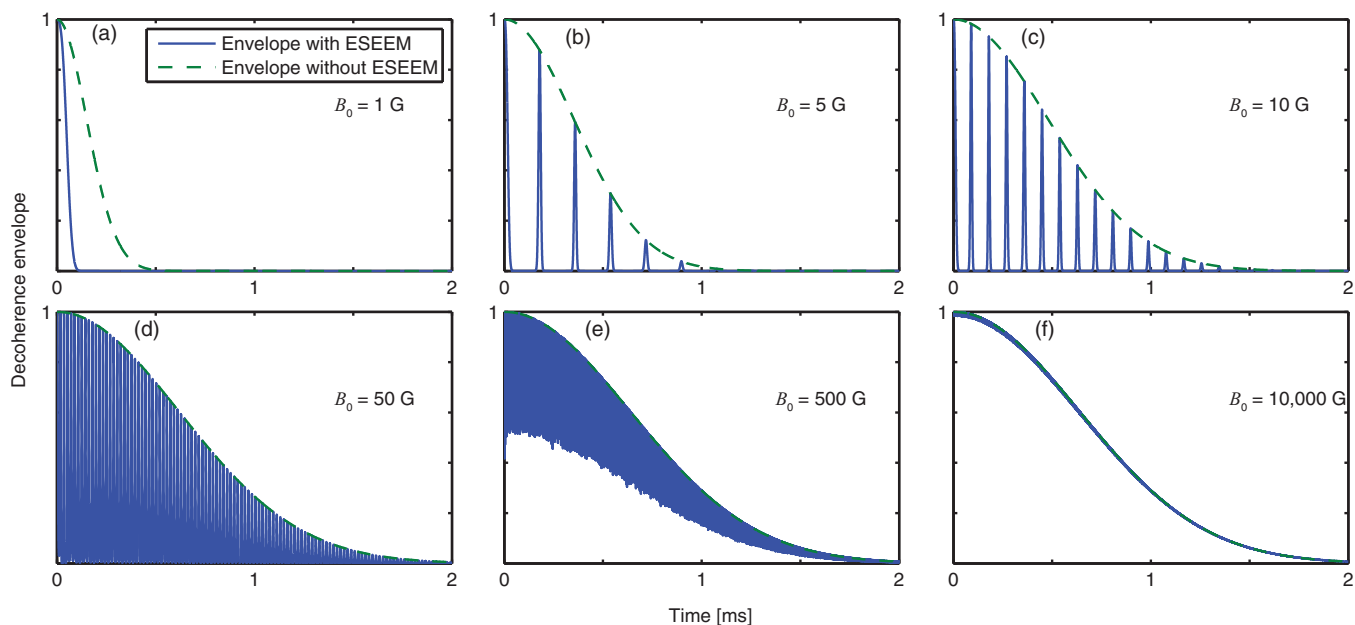


FIG. 15. (Color online) Plots showing the effect of electron spin-echo envelope modulation (ESEEM) on the decoherence envelopes of a NV center coupled to a 1.1% bath of ¹³C nuclear spin for different background magnetic field strengths. For extremely low fields (a), the revival rate is slower than the overall decoherence rate, leading to an apparent increase in decoherence. As the magnetic field is increased, as in (b)–(d), the revival rates increase proportionally, and the peak width decrease as $T_W \sim B_0^{-2/3}$. At high magnetic fields (e), the depths of the revivals begin to decrease, until they eventually disappear (f).

E. Analysis of the electron spin-echo envelope modulation (ESEEM)

One of the key features observed in experiments conducted on NV spins in ultrapure diamond is the emergence of decays and revivals in the spin-echo envelope at half the Larmor frequency of the ^{13}C spins [64], an effect referred to as electron spin-echo envelope modulation, or ESEEM (see Fig. 15). To this point, we have only concerned ourselves with the decoherence arising from flip-flop processes in the bath and have ignored the ESEEM contribution to the evolution. In this section, we analyze this effect and show how resulting properties such as the revival frequency, decay depth, and revival peak width depend on the background magnetic field strength. For background field strengths below approximately $B_0 = 1$ G, the revival frequency $\omega_R = \frac{1}{2}\gamma_c B_0 = 1.75$ kHz is lower than the decoherence rate. As such, the notion of a decay depth no longer makes sense, as there will be no subsequent revival before decoherence has occurred. In the following, we derive the analytic origins of these scalings.

Where the oscillations in the FID envelope occurred at the Larmor frequency ω_0 , the revival frequency during a spin-echo sequence is one half of the Larmor frequency, $\omega_R = \frac{1}{2}\gamma_E B_0 = 17.5 \text{ MHz T}^{-1} B_0$. Some broadening of this effect will occur due to the distribution of axial dipolar couplings in the bath, leading to a perceived increase in the decoherence rate; however, this effect will be addressed in the following section.

Next, we detail the dependence of the depth of the decay valleys on the magnetic field strength. A numerical calculation of the maximum amplitude of the ESEEM component of the decoherence function $|\Lambda^{(\text{ESEEM})}(t)|_{\text{max}}$ is plotted in Fig. 16(a). From this, we see that the decay depths scale with the inverse

square of the magnetic field strength at high fields, but only with the inverse at moderate field strengths.

Recall from Eq. (A23) that in the ZSE limit, the ESEEM correction to Λ_{ZSE} due to a single nuclear spin is given by

$$\Lambda_{\text{ZSE}}^{(\text{ESEEM})} = 4 \frac{A_x^2 + A_y^2}{\omega^2} \sin^2 \left[(A_z + \omega) \frac{t}{4} \right] \sin^2 \left(\frac{t\omega}{4} \right). \quad (42)$$

As this correction has been calculated in the $\omega \gg A$ limit, we must distinguish between cases where all spins are in the ZSE regime, and cases where distant spins from the NV are in the ZSE regime, but closer spins are in the SZE regime due to their dominant hyperfine interaction. For the former case, we have that the Zeeman coupling is greater than the most strongly coupled nuclear spin (i.e., where $B_0 > 162$ G), giving

$$\begin{aligned} |\Lambda_{\text{ZSE}}^{(\text{ESEEM})}|_{\text{max}} &= -4 \left\langle \frac{A_x^2 + A_y^2}{\omega^2} \right\rangle \\ &= -\frac{2}{15} \left(8\pi \frac{an}{\omega} \right)^2 = -\left(\frac{354 \text{ G}}{B_0} \right)^2, \end{aligned} \quad (43)$$

thus reproducing the $\sim \mathcal{O}(B_0^{-2})$ scaling of the numerical result, as plotted in Fig. 16(a).

For the case where the field strength is low enough to have spins in both the ZSE and SZE regimes, we must determine the contribution from both. The ZSE contribution to the decay may be determined by integrating Eq. (42) over only the spins in this regime. To determine the SZE contribution, we expand the ESEEM terms for $\omega \ll A$ as given in

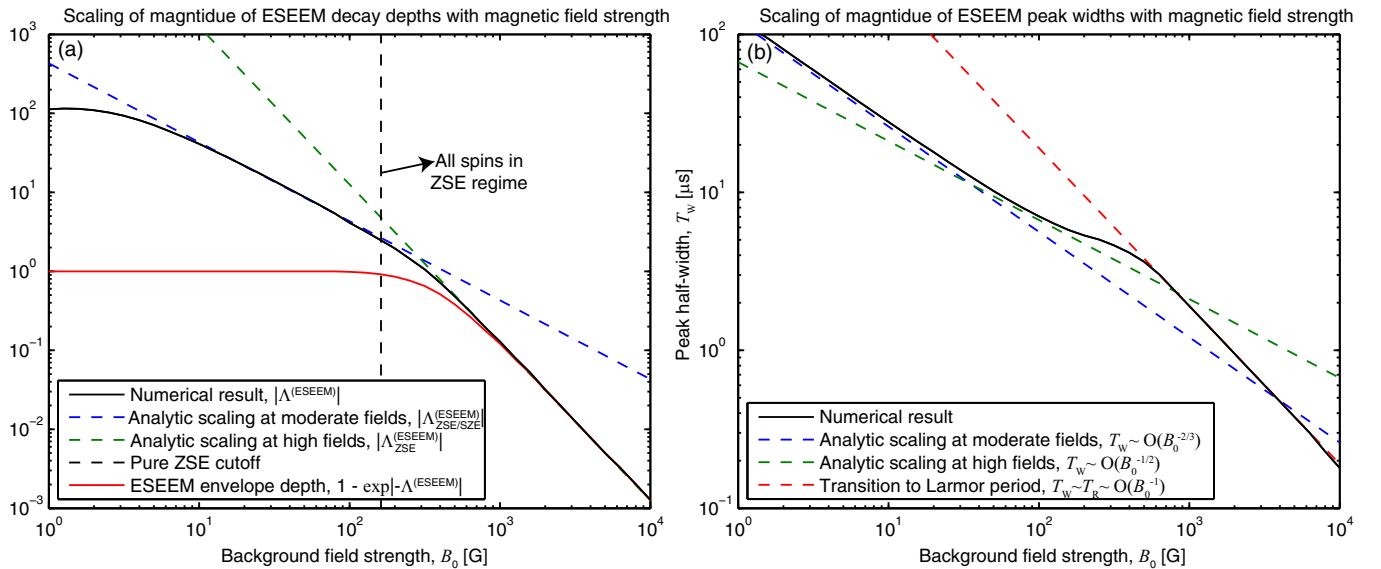


FIG. 16. (Color online) Magnetic field dependence of ESEEM features. (a) Plot detailing the magnitude of the modulation of the decoherence function. The numerical result is plotted in black, whereas the moderate and high-field analytic limits are plotted in blue and green, respectively. The saturation of the numerical result at low fields arises because the revival rate has decreased below the decoherence rate, which also saturates at low field. The red curve shows the magnitude of the corresponding spin-echo envelope contrast due to ESEEM, $1 - L = 1 - \exp(-\Lambda^{(\text{ESEEM})})$, which saturates at unity when the decoherence function is greater than unity. (b) Plot detailing the dependence of the width of the ESEEM peaks on the magnetic field strength. The numerical result is plotted in black, and the low-, moderate-, and high-field analytic results are plotted in blue, green, and red, respectively. In the case of the high-field result, the decay depth is less than unity, hence the width of the peaks is defined by the revival period instead of the decay time.

Eq. (A24):

$$\Lambda_{\text{SZE}}^{(\text{ESEEM})} = 4 \frac{A_{x,1}^2 + A_{y,1}^2}{A_1^2} \left[1 - \frac{2\omega A_{z,1}}{A_1^2} \right] \times \sin^2\left(\frac{t\lambda_1}{4}\right) \sin^2\left(\frac{t\omega}{4}\right), \quad (44)$$

and integrate over only the spins in the SZE regime. The sum of these two contributions gives

$$\begin{aligned} |\Lambda_{\text{ZSE/SZE}}^{(\text{ESEEM})}|_{\text{max}} &= \frac{32\pi an}{5\omega} + \frac{448\pi(5\sqrt{3}\pi - 27)an}{135\omega} \\ &= \frac{860 \text{ G}}{B_0}, \end{aligned} \quad (45)$$

again in agreement with the numerical result [see Fig. 16(a)].

Finally, we analyze the dependence of the decay widths T_w on the magnetic field. The numerical results in plotted in Fig. 16(b) show these widths to scale as $T_w \sim B_0^{-0.67}$ at moderate fields, as consistent with the scaling of $B_0^{-0.63}$ in the numerical results of Ref. [59]. At high fields, our numerical results show a slight change in this scaling for a brief period, with $T_w \sim B_0^{-1/2}$. If the magnetic field is increased further, the decay depths will be less than unity [see Fig. 16(a)], meaning the widths will be effectively characterized by half the revival period $T_w \sim \frac{1}{2}T_R$, showing an inverse linear dependence on the magnetic field strength, again consistent with the numerical results. We do not consider the low-field regimes, as revivals are not visible prior to the onset of decoherence. The analytic origins of these results are discussed in the following.

In the high-field (ZSE) limit, we expand Eq. (42) about any of the revival peaks, giving

$$\begin{aligned} \langle \Lambda_{\text{ZSE}}^{(\text{ESEEM})} \rangle &= \left\langle \frac{1}{64} t^4 (A_{x,1}^2 + A_{y,1}^2) (A_{z,1} + \omega)^2 \right\rangle \\ &\sim \frac{1}{30} \pi^2 a^2 n^2 t^4 \omega^2, \end{aligned} \quad (46)$$

giving a decay width of $T_w = 61 \mu\text{s G}^{1/2} / \sqrt{B_0}$.

To find the decay widths at low fields, we integrate Eq. (44). This puts us in a regime where $\omega \ll an$, meaning we must integrate the resulting expression over \mathbf{R} , and then expand for $1/an \ll t \ll 1/\omega$, giving

$$\begin{aligned} \langle \Lambda_{\text{SZE}}^{(\text{ESEEM})} \rangle &= \left\langle \frac{\omega^2 t^2 (A_{x,1}^2 + A_{y,1}^2) \sin^2\left(\frac{1}{4}A_1 t\right)}{4A_1^2} \right\rangle \\ &\sim \frac{1}{192} \pi^2 a n t^3 \omega^2 [18 - 5\sqrt{3} \cosh^{-1}(2)], \end{aligned}$$

showing the revival peaks to have a cubic shape. The resulting peak width is then

$$T_w^{(\text{SZE})} = \frac{121 \mu\text{s G}^{2/3}}{B_0^{2/3}}. \quad (47)$$

While this result is consistent with both the numerical work of our own, and that of Ref. [59], it differs from the analysis given in Ref. [64], which claims a quartic shape for the peaks, leading to a $T_w^{(\text{SZE})} \sim \mathcal{O}(B_0^{-1/2})$ dependence at moderate fields. This analysis was performed using a short-time expansion with respect to both Zeeman and hyperfine couplings, however,

such an expansion is not valid in the SZE regime where short time with respect to $T_R \sim 1/\omega$ is still long compared with $T_2^* \sim 1/an$.

VIII. ON THE QUESTION OF WHETHER THE NUCLEAR SPIN BATH MAY BE MODELED AS A CLASSICAL MAGNETIC FIELD

In treating the influence of the surrounding spin bath on a central spin, one commonly adopted approach [10,13,27–34] is to replace the collective hyperfine field felt by the NV spin with a semiclassical magnetic field whose internal dynamics are dictated by the autocorrelation functions discussed above. This field, the operator of which is denoted $\mathcal{B}(t)$, will produce a time-dependent Zeeman shift given by $\mathcal{H}_z = \vec{B} \cdot \vec{S} \equiv S_z B(t)$ and a corresponding free-time evolution operator of

$$\mathcal{U}_f(t', t'') = e^{-i\phi(t', t'')} |1\rangle\langle 1| + |0\rangle\langle 0|, \quad (48)$$

where $\phi(t', t'') = \int_{t'}^{t''} B(t) dt$. Such an approach is potentially problematic, as it ignores the effect of the hyperfine couplings on the evolution of the nuclei, which as we have shown are a critical component of this evolution.

The phase shift of the central spin will always depend on the pulse sequence employed, but a certain degree of abstraction is achieved if we consider the second integral of the environmental autocorrelation function G , defined by

$$\frac{d^2}{dt^2} G(t) = \langle B(t') B(t'') \rangle. \quad (49)$$

It then becomes a simple exercise to show, using Eq. (E5), the pulse-sequence-specific decoherence functions are given by appropriate linear combinations of dilated G functions,

$$\begin{aligned} \Lambda_{\text{FID}} &= \frac{1}{2} \langle \phi_{\text{FID}}^2(t) \rangle = G(t), \\ \Lambda_{\text{se}} &= \frac{1}{2} \langle \phi_{\text{se}}^2(t) \rangle = 4G(t/2) - G(t), \end{aligned} \quad (50)$$

and so on, showing that G essentially plays the role of a classical “generalized decoherence function.”

Using the secular autocorrelation function [Eq. (C3)], we find the corresponding semiclassical spin-echo decoherence function for the ZSE regime to be

$$\begin{aligned} \Lambda &\sim \frac{128 \sqrt[3]{2} (4 - \sqrt[3]{2}) \pi^{14/3} (ant)^2 (bnt)^{5/3}}{45 \cdot 3^{2/3} \Gamma\left(\frac{14}{3}\right)} \\ &\quad - \frac{64\pi^5 (ant)^2 (bnt)^2}{135 \sqrt{3} \Gamma\left(\frac{4}{3}\right)} \\ &= \left(\frac{t}{120 \mu\text{s}}\right)^{11/3} - \left(\frac{t}{180 \mu\text{s}}\right)^4, \end{aligned} \quad (51)$$

giving a coherence time of 127 μs . Notice that the effective magnetic field emanating from the lateral components of the nuclear spins has been suppressed to order $A_{x,y}^2/\omega^2$ by virtue of double integration with respect to t of terms involving $\cos(\omega t)$, leaving only $z-z$ components of the effective field in the $Z > E$ limit. This is consistent with the suppression of lateral components seen in the transition from SZE to ZSE regimes in the quantum mechanical analysis of this work.

Similarly, using the nonsecular autocorrelation function [Eq. (C7)], the semiclassical spin-echo decoherence

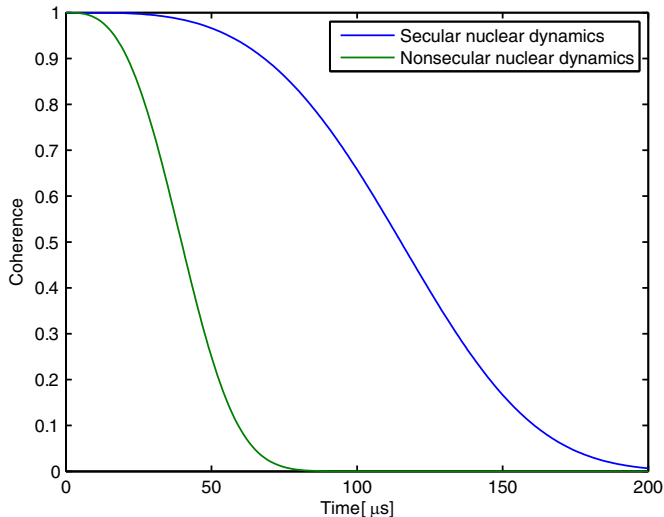


FIG. 17. (Color online) Plots showing the decoherence envelopes calculated using a semiclassical approach based on the determination of the autocorrelation function of the effective magnetic field from the hyperfine coupling of the environmental nuclei to the central spin. Qualitatively, this approach reproduces the effect of increasing the magnetic field, in that the decoherence rates are much faster for a nonsecular environmental regime than those of a secular regime. However, the resulting coherence times are nearly an order of magnitude shorter than those computed with the quantum mechanical approach developed in this work, resulting from a mistreatment of the hyperfine couplings, ultimately showing that a semiclassical treatment of this problem is not adequate.

function corresponding to the SEZ regime is

$$\Lambda = \frac{64}{243} \pi^4 (ant)^2 bnt, \quad (52)$$

which has an associated coherence time of 45 μ s.

The resulting spin-echo envelopes from this semiclassical analysis are plotted in Fig. 17. From these results, we see that the associated coherence times are almost an order of magnitude shorter than those deduced using the quantum mechanical approach developed in this work. We can attribute this discrepancy to the semiclassical approach not taking into account the backaction of the central spin on the environment, leading to a number of consequences.

First, this allows for the environment to evolve freely under its own influence at all times, irrespective of the spin state (and hence the projected hyperfine field) of the NV, essentially doubling the effective fluctuation rate of the semiclassical spin-bath field. In previous work [23], we have shown that this increases the spin-echo decoherence rate for systems that exist in a slowly fluctuating regime, as is the case for the nuclear spin bath considered here.

Second, the semiclassical approach overestimates the dependence of the scaling of the temporal scalings of the resulting decoherence functions, leading to scalings of $\Lambda \sim t^{11/3}$ and $\Lambda \sim t^3$ associated with the secular and nonsecular nuclear dynamics. This is again in contrast to the quantum mechanical results, which show quadratic scalings for the three parameter regimes applicable to this problem.

The third consequence is more critical. Whereas in the quantum mechanical analysis, the hyperfine coupling entered

into the decoherence function as $\sin^2(A_z t/4)$, in the semiclassical case the hyperfine coupling manifests as $(A_z t)^2$, showing the latter to correspond to the short-time limit of the former. This means the two approaches only agree on time scales that are shorter than the FID time, implying that the semiclassical approach is not valid in analyzing the spin-echo decay of a NV center coupled to a nuclear spin.

IX. CONCLUSION

In this work, we have developed a quantum mechanical methodology by which to analytically treat the decoherence of a NV center spin coupled to a nuclear spin environment. This approach, based on the microscopic spatial statistics of environmental impurities, affords a natural decomposition of the bath into six distinct parameter regimes as defined by the relative strengths of the hyperfine, Zeeman, and mutual dipolar coupling of the environmental spins, and avoids the need for *ad hoc* assumptions regarding the environmental NV-nuclear or nuclear-nuclear dynamics. This allows us to explicitly determine the analytic form of the associated decoherence functions in several regimes relevant to current experiments, and to derive the dependence of quantities such as coherence times and characteristic ESEEM features on the strength of a background magnetic field. In doing so, we have demonstrated excellent agreement with existing numerical and experimental work.

ACKNOWLEDGMENTS

The authors would like to thank D. A. Simpson, C. D. Hill, J. Wrachtrup, H. Fedder, F. Jelezko, L. P. McGuinness, B. Naydenov, and V. Jaques for helpful discussions. This work was supported by the Australian Research Council under the Centre of Excellence scheme (Project No. CE110001027).

APPENDIX A: SINGLE-CLUSTER DYNAMICS AND DECOHERENCE

Since the evolution during a free-precession interval is so heavily dependent on the NV spin state, we can project this Hamiltonian along both basis states. Thus,

$$\mathcal{H} \equiv |1\rangle\langle 1| \mathcal{H}_1 + |0\rangle\langle 0| \mathcal{H}_0. \quad (A1)$$

Because no hyperfine coupling exists when the NV is in the $|0\rangle$ state, projection onto the distinct NV states allows us to distinguish between the Hamiltonians associated with the $|0\rangle$ and $|+1\rangle$ states, namely, \mathcal{H}_0 and \mathcal{H}_1 , respectively.

For a FID experiment, the time-evolution operator is given by

$$\begin{aligned} \mathcal{U}_{\text{FID}}(t) &= |1\rangle\langle 1| \otimes \exp(-i\mathcal{H}_1 t) + |0\rangle\langle 0| \otimes \exp(-i\mathcal{H}_0 t) \\ &\equiv |1\rangle\langle 1| \otimes \mathcal{U}_1(t) + |0\rangle\langle 0| \otimes \mathcal{U}_0(t), \end{aligned} \quad (A2)$$

where $\mathcal{U}_1(t)$ and $\mathcal{U}_0(t)$ are the projections of the time-evolution operator onto the $|+1\rangle$ and $|0\rangle$ states of the NV spin, respectively.

In general, we wish to consider the effect of different pulse sequences, which involve periods of free evolution followed by applied pulses at particular times. A general time-evolution operator will contain exponents of the above Hamiltonians,

however, these exponents will appear as different components of the 2×2 matrix describing the central spin, depending on the pulse sequence considered. To keep things general, we write

$$\mathcal{U}(t) = \begin{pmatrix} \mathcal{K}_{11}(t) & \mathcal{K}_{10}(t) \\ \mathcal{K}_{01}(t) & \mathcal{K}_{00}(t) \end{pmatrix}, \quad (\text{A3})$$

however, just what the $\mathcal{K}_{mn}(t)$ are will depend on the pulse sequence employed. For the FID case just mentioned, we just simply have $\mathcal{K}_{11}(t) = \mathcal{U}_1(t)$, $\mathcal{K}_{00}(t) = \mathcal{U}_0(t)$, $\mathcal{K}_{10}(t) = \mathcal{K}_{01}(t) = 0$.

The relatively short coherence times of a FID experiment may be extended by 2–4 orders of magnitude by applying an appropriate sequence of π pulses (or bit-flips, denoted \mathcal{F}), under which the quantum amplitudes of the $|1\rangle$ and $|0\rangle$ states are swapped. In the simplest instance, we consider a Hahn-echo or spin-echo pulse sequence, involving a single- π pulse applied at time $t/2$. The effect of this sequence is to refocus any static components of the bath, thereby extending coherence times by roughly 2 orders of magnitude, with typical times of 400 μs ms. The time-evolution operator for a spin-echo experiment is

$$\mathcal{U}_{\text{SE}}(t) = \mathcal{U}_{\text{FID}}(t/2) \mathcal{F} \mathcal{U}_{\text{FID}}(t/2), \quad (\text{A4})$$

hence we make the identification

$$\begin{aligned} \mathcal{K}_{10}(t) &= \mathcal{U}_1(t/2) \mathcal{U}_0(t/2), \\ \mathcal{K}_{01}(t) &= \mathcal{U}_0(t/2) \mathcal{U}_1(t/2), \\ \mathcal{K}_{11}(t) &= \mathcal{K}_{00}(t) = 0. \end{aligned} \quad (\text{A5})$$

The density matrix $\rho(t)$ at $t = 0$ is given by

$$\rho(0) = [|1\rangle\langle 1| + |1\rangle\langle 0| + |0\rangle\langle 1| + |0\rangle\langle 0|] \otimes \mathcal{M}_{\text{E}},$$

where \mathcal{M}_{E} denotes a purely mixed environmental state. The in-plane magnetization at time t is found from

$$L = \text{Tr}\{(\mathcal{S}_x + i\mathcal{S}_y)\rho(t)\}. \quad (\text{A6})$$

From this, we see that the FID and spin-echo signals are given by

$$\begin{aligned} L_{\text{FID}} &= \frac{1}{2^k} \text{Tr}_{\text{E}}\{\mathcal{U}_0(t) \mathcal{U}_1^\dagger(t)\}, \\ L_{\text{SE}} &= \frac{1}{2^k} \text{Tr}_{\text{E}}\{\mathcal{U}_0(t/2) \mathcal{U}_1(t/2) \mathcal{U}_0^\dagger(t/2) \mathcal{U}_1^\dagger(t/2)\}, \end{aligned} \quad (\text{A7})$$

respectively, where k is the number of spins in the cluster. The exact forms of the propagators will be determined by the regime in question, allowing us to make asymptotic expansions in terms of the relative coupling scales, such as an/ω , bn/ω , and a/b , where n is the density of the spins in the bath.

1. Environmental autocorrelation functions and frequency spectra

a. Secular nuclear dynamics

The full effective axial magnetic field operator as felt by the central spin is due to the axial components of the hyperfine

interaction

$$\mathcal{B}_2 = \sum_{j=1}^{N_k} (A_{zx}^{(j)} \mathcal{E}_x^{(j)} + A_{zy}^{(j)} \mathcal{E}_y^{(j)} + A_{zz}^{(j)} \mathcal{E}_z^{(j)}), \quad (\text{A8})$$

where N_k is the number of spins in the k th cluster. For $n_k = 2$, this leads to an autocorrelation function of

$$\begin{aligned} \langle \mathcal{B}_2(t) \mathcal{B}_2(0) \rangle_{\text{S}} &= A_{z,1}^2 + A_{z,2}^2 + (A_{x,1}^2 + A_{x,2}^2 + A_{y,1}^2 + A_{y,2}^2) \\ &\quad \times \cos(t\omega) - [\Delta_z^2 + (\Delta_x^2 + \Delta_y^2) \cos(t\omega)] \\ &\quad \times \sin^2\left(\frac{B_{12}t}{2}\right), \end{aligned} \quad (\text{A9})$$

where $\Delta_{x,y,z} \equiv |A_{x,y,z,1} - A_{x,y,z,2}|$.

These methods may be extended to obtain corrections for three spin interactions and higher. However, despite being interested in the short-time and relatively weak coupling to the next-nearest neighbor, we cannot use perturbation theory, as the couplings strengths still become infinite as the next-nearest-neighbor separation goes to zero. A short-time expansion of Eq. (A9) would diverge as r approaches 0, hence, to use perturbation theory at a given order for all possible geometric configurations (particularly when $B_{12}^2 \gg A_{z,1}^2 + A_{z,2}^2$, which defines the high frequency, and hence short-time behavior of the dynamics), we require the leading order of the relevant probability density function to be at least $\mathcal{O}\{r^4\}$. As we will see in Appendix B, this corresponds to the third-nearest neighbor and above. Hence, perturbation theory cannot be applied until cluster sizes of four or greater are considered.

In analyzing the dynamics of a three-spin cluster, we initially assume that a strongly coupled pair exists, and introduce a third impurity whose coupling to the initial two is comparatively weak. We assume the two couplings involving the third spin are of similar order and make small perturbations about this condition. This is justified by the rapid falloff of the dipole-dipole coupling, which ensures that any large deviation from this condition will yield a two-spin cluster and an effectively separate, uncoupled spin. From this, we find the autocorrelation function of a single three-spin cluster to be

$$\begin{aligned} \langle \mathcal{B}_3(t) \mathcal{B}_3(0) \rangle_{\text{S}} &= \langle \mathcal{B}_2(t) \mathcal{B}_2(0) \rangle_{\text{z}} + A_{z3}^2 - \frac{4}{9} \left[\Delta_{13} \sin^2\left(\frac{3B_{13}t}{4}\right) \right. \\ &\quad \left. + \Delta_{23} \sin^2\left(\frac{3B_{23}t}{4}\right) \right] \\ &\quad + \text{Larmor terms}. \end{aligned} \quad (\text{A10})$$

This result exhibits almost identical properties to the two-spin cluster case, with a persistent static component, and fluctuating components whose amplitudes are again proportional to the respective hyperfine coupling differences.

b. Nonsecular nuclear dynamics

The Hamiltonian describing the dipolar coupling between two spins when all possible terms are included is given by

$$\mathcal{H}_{\text{N}} = \frac{b}{r^3} \left[\vec{\mathcal{E}}_1 \cdot \vec{\mathcal{E}}_2 - \frac{3}{r^2} (\mathbf{r} \cdot \vec{\mathcal{E}}_1) (\mathbf{r} \cdot \vec{\mathcal{E}}_2) \right], \quad (\text{A11})$$

which yields the following nonsecular autocorrelation function of the axial magnetic field:

$$\begin{aligned} \langle \mathcal{B}_z(t)\mathcal{B}_z(0) \rangle_N &= (A_{z1}^2 + A_{z2}^2) \left[1 - \frac{4}{3} \sin^2 \left(\frac{3B_{12}t}{4} \right) \right] \\ &\quad - \frac{2}{3} \Delta_z^2 \left[\sin^2 \left(\frac{B_{12}t}{4} \right) + \frac{1}{2} \sin^2 \left(\frac{B_{12}t}{2} \right) \right] \\ &\quad - \sin^2 \left(\frac{3B_{12}t}{4} \right). \end{aligned} \quad (\text{A12})$$

2. Single-spin clusters and free-induction decay

Single-spin clusters, by definition, do not include any interaction with adjacent spins. The hyperfine and Zeeman coupling components of the Hamiltonian as projected onto the $|0\rangle$ and $|+1\rangle$ states of the NV spin are given by

$$\mathcal{H}_1 = A_x \mathcal{E}_x + A_y \mathcal{E}_y + (A_z + \omega) \mathcal{E}_z, \quad \mathcal{H}_0 = \omega \mathcal{E}_z, \quad (\text{A13})$$

from which we determine the FID and spin-echo envelopes using Eq. (A7):

$$L_{\text{FID}} = \cos \left(\frac{t\lambda}{2} \right) \cos \left(\frac{t\omega}{2} \right) + \frac{\Omega}{\lambda} \sin \left(\frac{t\lambda}{2} \right) \sin \left(\frac{t\omega}{2} \right), \quad (\text{A14})$$

$$L_{\text{SE}} = 1 - 2 \frac{A_x^2 + A_y^2}{\lambda^2} \sin^2 \left(\frac{t\lambda}{2} \right) \sin^2 \left(\frac{t\omega}{2} \right), \quad (\text{A15})$$

where $\Omega = A_z + \omega$ and $\lambda = \sqrt{A_x^2 + A_y^2 + \Omega^2}$. In this section, we will examine the behavior of these expressions in cases of high and low magnetic fields, however, one can immediately see that there is no spin-echo decoherence at both $\omega \rightarrow 0$ and $\omega \rightarrow \infty$ limits. This is in direct contrast with experimental observations, where the decoherence rate is maximal at zero field, and decreases to a final, constant value at sufficiently high magnetic fields. This implies that we must introduce more complex spin-spin interactions to be able to explain this discrepancy. Higher-order clusters are considered in the following sections, hence, in this section we focus solely on FID behavior.

Expanding the above result for $\omega \gg A_z$, we find the contribution to the FID from a single spin to be

$$\begin{aligned} L_{\text{FID}}^{(1)}|_{\omega \gg A} &\sim \cos \left(\frac{A_z t}{2} \right) - \frac{A_x^2 + A_y^2}{2\omega^2} \sin^2 \left(\frac{\omega t}{2} \right) \sin^2 \left(\frac{1}{2}(A_z + \omega)t \right), \end{aligned} \quad (\text{A16})$$

and in the low-field limit ($\omega \ll A_z$) we find

$$\begin{aligned} L_{\text{FID}}|_{\omega \ll A} &\sim \cos \left(\frac{At}{2} \right) \cos \left(\frac{\omega t}{2} \right) + \left[\frac{A_z}{A} + \frac{\omega(A_x^2 + A_y^2)}{A^3} \right. \\ &\quad \left. - \frac{3\omega^2(A_x^2 + A_y^2)A_z}{2A^5} \right] \sin \left(\frac{At}{2} \right) \sin \left(\frac{\omega t}{2} \right), \end{aligned} \quad (\text{A17})$$

where $A = \sqrt{A_x^2 + A_y^2 + A_z^2}$.

3. Two-spin clusters and spin-echo decay

In this section, we discuss how the full Hamiltonian [Eq. (2)] may be simplified according to the parameter regimes in question to solve for the corresponding evolution.

a. Secular dipole-dipole coupling with nonsecular hyperfine coupling (ZSE), and secular dipole-dipole coupling (SZE)

As discussed earlier, when the NV spin is in the $|+1\rangle$ state, the difference in the hyperfine couplings will yield sufficient detuning to suppress any dipolar flip-flops, hence, we may ignore the dipolar term in the projection of the Hamiltonian on the $|+1\rangle$ spin state. Furthermore, the fact that the Zeeman terms are much greater than the dipolar terms allows us to ignore spin-spin interactions that do not conserve total magnetization with respect to the background field $\vec{\omega}$ and make the secular approximation for the dipole-dipole coupling. Thus, the relevant Hamiltonians for the ZSE and SZE regimes are given by

$$\begin{aligned} \mathcal{H}_1 &= \sum_{k=1}^2 [A_{x,k} \mathcal{E}_{x,k} + A_{y,k} \mathcal{E}_{y,k} + (A_{z,k} + \omega) \mathcal{E}_{z,k}], \\ \mathcal{H}_0 &= B(\mathcal{E}_{x,1} \mathcal{E}_{x,2} + \mathcal{E}_{y,1} \mathcal{E}_{y,2} - 2\mathcal{E}_{z,1} \mathcal{E}_{z,2}) + \omega(\mathcal{E}_{z,1} + \mathcal{E}_{z,2}). \end{aligned} \quad (\text{A18})$$

Using Eq. (A7), the full spin-echo decoherence envelope of the NV spin due to a two-spin cluster undergoing a secular flip-flop process is given below in Eq. (A19). This expression is exact, and the ZSE and SZE analytic limits have been employed in the main text. This envelope will contain contributions from flip-flop (FF, lateral and longitudinal), precession (P, lateral only), and simultaneous flip-flop and precession (FF-P) processes. For clarity, we outline these contributions separately, whence

$$L_{\text{sec}} = 1 + L_{\text{FF}} + L_{\text{P}} + L_{\text{FF-P}}. \quad (\text{A19})$$

The precession component is responsible for the decays and revivals at moderate magnetic fields, and is given by

$$\begin{aligned} L_{\text{P}} &= -2 \frac{A_{x,1}^2 + A_{y,1}^2}{\lambda_1^2} \sin^2 \left(\frac{\lambda_1 t}{4} \right) \sin^2 \left(\frac{\omega t}{4} \right) - 2 \frac{A_{x,2}^2 + A_{y,2}^2}{\lambda_2^2} \sin^2 \left(\frac{\lambda_2 t}{4} \right) \sin^2 \left(\frac{\omega t}{4} \right) \\ &\quad + 4 \frac{(A_{x,1}^2 + A_{y,1}^2)(A_{x,2}^2 + A_{y,2}^2)}{\lambda_1^2 \lambda_2^2} \sin^2 \left(\frac{\lambda_1 t}{4} \right) \sin^2 \left(\frac{\lambda_2 t}{4} \right) \sin^4 \left(\frac{\omega t}{4} \right), \end{aligned} \quad (\text{A20})$$

the flip-flop processes are responsible for the decoherence of the NV spin,

$$L_{\text{FF}} = \frac{A_{x,1}A_{x,2} + A_{y,1}A_{y,2} + \Omega_1\Omega_2}{2\lambda_1\lambda_2} \sin^2\left(\frac{Bt}{4}\right) \sin\left(\frac{t\lambda_1}{2}\right) \sin\left(\frac{t\lambda_2}{2}\right) - \frac{1}{2} \sin^2\left(\frac{Bt}{4}\right) \left[1 - \cos\left(\frac{t\lambda_1}{2}\right) \cos\left(\frac{t\lambda_2}{2}\right)\right] \\ - 2 \frac{(A_{x,2}A_{y,1} - A_{x,1}A_{y,2})^2 + (\Omega_1A_{x,2} - \Omega_2A_{x,1})^2 + (\Omega_1A_{y,2} - \Omega_2A_{y,1})^2}{\lambda_1^2\lambda_2^2} \sin^2\left(\frac{Bt}{4}\right) \sin^2\left(\frac{t\lambda_1}{4}\right) \sin^2\left(\frac{t\lambda_2}{4}\right), \quad (\text{A21})$$

and the hybrid processes are described by

$$L_{\text{FF-P}} = 2 \frac{(\Omega_1A_{x,2} - \Omega_2A_{x,1})^2 + (\Omega_1A_{y,2} - \Omega_2A_{y,1})^2}{\lambda_1^2\lambda_2^2} \sin^2\left(\frac{Bt}{4}\right) \sin^2\left(\frac{t\lambda_1}{4}\right) \sin^2\left(\frac{t\lambda_2}{4}\right) \sin^2\left(\frac{t\omega}{4}\right) \\ - \frac{A_{x,1}A_{x,2} + A_{y,1}A_{y,2}}{\lambda_1\lambda_2} \sin^2\left(\frac{Bt}{4}\right) \sin\left(\frac{t\lambda_1}{2}\right) \sin\left(\frac{t\lambda_2}{2}\right) \sin^2\left(\frac{t\omega}{4}\right) \\ + 2 \frac{A_{x,1}^2 + A_{y,1}^2}{\lambda_1^2} \sin^2\left(\frac{Bt}{4}\right) \sin^2\left(\frac{t\lambda_1}{4}\right) \cos^2\left(\frac{t\lambda_2}{4}\right) \sin^2\left(\frac{t\omega}{4}\right) \\ + 2 \frac{A_{x,2}^2 + A_{y,2}^2}{\lambda_2^2} \sin^2\left(\frac{Bt}{4}\right) \sin^2\left(\frac{t\lambda_2}{4}\right) \cos^2\left(\frac{t\lambda_1}{4}\right) \sin^2\left(\frac{t\omega}{4}\right). \quad (\text{A22})$$

Using this result, and expanding to second order for small $A_{x,y,z}/\omega$, we obtain the contribution to the spin-echo decoherence of the central spin due to a two-spin cluster:

$$L_{\text{ZSE}} = 1 - \sin^2\left(\frac{Bt}{4}\right) \sin^2\left(\frac{\Delta_z t}{4}\right) - \frac{\Delta_x^2 + \Delta_y^2}{\omega^2} \\ \times \sin^2\left(\frac{Bt}{4}\right) \sin^2\left[\left(A_{z,1} + \omega\right)\frac{t}{4}\right] \\ - 4 \frac{A_{x,1}^2 + A_{y,1}^2}{\omega^2} \sin^2\left[\left(A_{z,1} + \omega\right)\frac{t}{4}\right] \sin^2\left(\frac{t\omega}{4}\right). \quad (\text{A23})$$

We note that only the terms containing the dipole-dipole coupling B represent any actual decoherence, with the presence of a finite magnetic field increasing the effect by a factor of $1 + \frac{\Delta_x^2 + \Delta_y^2}{4\omega^2}$. The final term corresponds to the lateral dynamics (precession) of the nuclei, and hence does not contribute any decoherence, for reasons analogous to those discussed in Sec. A 2, however, it does detail the emergence of the decay/revival behavior seen in spin-echo experiments on electron spins coupled to nuclear spin baths. Specifically, we see that the amplitude of the revivals increases with decreasing magnetic field, as does their width.

Despite not contributing any true decoherence, the decays and revivals at the Larmor frequency are susceptible to inhomogeneous broadening from the axial couplings to all other spins in the bath, leading to an additional dephasing component in the evolution of the central spin. Such a distinction is important, as it explains the major difference between numerically calculated and experimentally observed behavior of this system. This effect is considered in detail in Sec. VII E. Further corrections to the Larmor broadening due to larger cluster sizes may be calculated iteratively by employing the spectral distribution when performing the ensemble average, however, these corrections will lead to

terms with a dependence on t beyond that of leading order and are thus not important.

As with the ZSE regime, the $|+1\rangle$ state of the NV spin yields sufficient detuning to suppress any dipolar flip-flops, hence, we may ignore the dipolar term in the projection of the Hamiltonian on the $|+1\rangle$ spin state. We are working in a regime where the Zeeman terms are still much greater than the dipolar terms, allowing us to ignore spin-spin interactions that do not conserve total magnetization with respect to the background field. Thus, the Hamiltonian, and hence the decoherence function for the SZE regime are identical to that for the ZSE regime; however, we instead expand Eq. (A21) for small $\omega/A_{x,y,z}^{1,2}$, giving

$$L_{\text{SZE}} = 1 - \sin^2\left(\frac{Bt}{4}\right) \sin^2\left(\frac{\Delta}{4}t\right) - 4 \frac{A_{x,1}^2 + A_{y,1}^2}{A_1^2} \\ \times \left[1 - \frac{2\omega A_{z,1}}{A_1^2}\right] \sin^2\left(\frac{t\lambda_1}{4}\right) \sin^2\left(\frac{t\omega}{4}\right) \\ + \frac{4(A_{x,1}^2 + A_{y,1}^2)^2}{A_1^4} \left[1 - \frac{4\omega A_{z,1}}{A_1^2}\right] \sin^4\left(\frac{t\lambda_1}{4}\right) \\ \times \sin^4\left(\frac{t\omega}{4}\right), \quad (\text{A24})$$

where $\Delta \equiv |A_1 - A_2|$. We note here that this expression is very similar to that of the ZSE regime, however, the effective hyperfine coupling strength has increased from Δ_z to Δ . This is a consequence of the quantization axis of the spins being set by their hyperfine coupling rather than their Zeeman coupling.

b. Strong, nonsecular hyperfine coupling, nonsecular dipole-dipole coupling (SEZ)

In this regime, we still have that the hyperfine couplings dominate when the NV is in the $|+1\rangle$ state. When the NV is in the $|0\rangle$ state, the dipolar couplings between the environmental spins will dictate the evolution, as with the

ZSE and SZE regimes; however, in this regime, the dipolar couplings dominate over the Zeeman terms. This means that the quantization axis of the spins is set by their mutual interaction, and the cluster is thus not required to conserve magnetization with respect to the background field. Including all possible dipole interaction terms, we have

$$\begin{aligned}\mathcal{H}_1 &= \sum_{k=1}^2 [A_{x,k} \mathcal{S}_{x,k} + A_{y,k} \mathcal{S}_{y,k} + (A_{z,k} + \omega) \mathcal{S}_{z,k}], \\ \mathcal{H}_0 &= B[\vec{S}_1 \cdot \vec{S}_2 - 3(\mathbf{n} \cdot \vec{S}_1)(\mathbf{n} \cdot \vec{S}_2)],\end{aligned}\quad (\text{A25})$$

where \mathbf{n} is the unit vector separating spins 1 and 2. The full spin-echo envelope for the SEZ regime is too large to reproduce here, however, we may simplify things immensely by averaging over the angular components of the cluster geometry (θ, ϕ) , giving

$$L_{\text{SEZ}} = 1 - \frac{8}{15} \sin^2\left(\frac{3Bt}{4}\right) \left[\sin^2\left(\frac{At}{2}\right) + \sin^2\left(\frac{At}{4}\right) \right], \quad (\text{A26})$$

where $A = \sqrt{A_x^2 + A_y^2 + A_z^2}$. Notice that the hyperfine coupling now emerges as A instead of Δ , which is a consequence of the magnetization no longer being conserved with respect to the background field. This results in a significantly larger fluctuation amplitude, as $\langle A^2 \rangle = (\frac{4\pi na}{3})^2$, whereas $\langle \Delta^2 \rangle = (2na)^2$. The separation of hyperfine and dipolar processes also means that we need not distinguish between A_1 and A_2 , as their relative locations are no longer important as far as the hyperfine component of the evolution is concerned. As the contributions of each spin will be summed over in an equivalent manner, we simply put $A_1 = A_2 = A$. This is in contrast to the ZSE and SZE cases, where the hyperfine couplings manifest as Δ_z and Δ , respectively, as the treatment of spin 2 will depend on the location of spin 1.

In the following Appendix, we discuss the statistics associated with the random distribution of spin impurities in a spin-bath environment. These statistics will be used to determine the combined effect on the coherence of the central spin from all clusters in the bath.

APPENDIX B: SPATIAL STATISTICS OF RANDOMLY DISTRIBUTED IMPURITIES

In this Appendix, we derive the probability density functions associated with the distance between the nearest-neighbor (NN), next-nearest-neighbor (NNN), and so forth, impurities in the environment. These distributions will be used to determine the collective dynamic behavior of the environment and allow us to compare the contributions from the different orders of clustering. We first consider the case of a continuum distribution, in which spin impurities may adopt any position in the lattice according to their spatial density. We then consider the specific case of NV centers in diamond, in which carbon atoms are arranged in a tetrahedral diamond lattice.

For a given lattice site density (or carbon atom number density) of n_c , the volume V concentric on any one environmental spin impurity contains $N \approx n_c V - 1$ sites that may be occupied by a second impurity. The probability of

finding X spins within V is then a binomial distribution with N -independent trials, with each site having a probability $\chi = 0.011$ of being occupied by a nucleus of nonzero spin:

$$P(X|N, \chi) \approx \frac{(V/V_0)!}{X!(V/V_0 - X)!} \chi^X (1 - \chi)^{V/V_0 - X}, \quad (\text{B1})$$

which, in the limit of low-spin concentrations $\chi \ll 1$, approaches a Poisson distribution

$$P(X|V, \chi) \approx \frac{1}{X!} (\zeta r^3)^X \exp(-\zeta r^3), \quad (\text{B2})$$

where $\zeta \equiv \frac{4\pi\chi}{3V_0}$, implying an average spin impurity density of $n = \chi/V_0$. The probability that a sphere concentric on a given environment spin contains at least one other spin is given by which, by definition, is also the cumulative probability function. As such, the probability of encountering a spin *at r* (i.e., on the shell of V) is given by

$$P(r) = \frac{d}{dr} P(X > 0, r) = 4\pi n r^2 \exp\left(-\frac{4\pi n r^3}{3}\right). \quad (\text{B3})$$

In other words, $P(r)$ is the probability density function for the distance between two nearest-neighbor spins.

This analysis may be extended to compute the probability distribution of the distance to the k th nearest neighbor. Consider the region bounded by concentric spheres of radii r_1 and r_0 , the volume of which is $\frac{4}{3}\pi(r_1^3 - r_0^3)$. As above, the probability that at least one impurity exists in this region is $1 - \exp[-\zeta(r_1^3 - r_0^3)]$, which has the corresponding probability density function

$$P(r_1) = 3\zeta r_1^2 \exp[-\zeta(r_1^3 - r_0^3)].$$

Similarly, the probability density function for the distance to the k th impurity is

$$P(r_k) = 3\zeta r_k^2 \exp[-\zeta(r_k^3 - r_{k-1}^3)].$$

Taking $r_0 = 0$, the joint probability density function is

$$P(r_1, \dots, r_k) = \prod_{j=1}^k p_r(r_j) = (3\zeta)^k r_1^2 \dots r_k^2 \exp[-\zeta r_k^3].$$

To obtain the distribution for each r_j , we successively integrate over all $r_1, \dots, r_{j-1}, r_{j+1}, \dots, r_k$ from 0 to r_{j+1} .

Thus, given the location of some environmental spin, the probability of finding its k th nearest neighbor at a distance of r_k is given by

$$P_k(r_k) = \frac{4\pi n r_k^2}{(k-1)!} \left(\frac{4\pi n r_k^3}{3}\right)^{k-1} \exp\left[-\frac{4\pi n r_k^3}{3}\right]. \quad (\text{B4})$$

Computing the first and second moments of this distribution, we find

$$\langle r_k \rangle = \left(\frac{4\pi n}{3}\right)^{-\frac{1}{3}} \frac{\Gamma(k + \frac{1}{3})}{(k-1)!} \quad (\text{B5})$$

and

$$\langle r_k^2 \rangle = \left(\frac{4\pi n}{3}\right)^{-\frac{2}{3}} \frac{\Gamma(k + \frac{2}{3})}{(k-1)!}. \quad (\text{B6})$$

A plot of the mean distance to the first 10 nearest neighbors, $\langle r_k \rangle$ for $k = 1, \dots, 10$, is shown in Fig. 18(b). This quantity

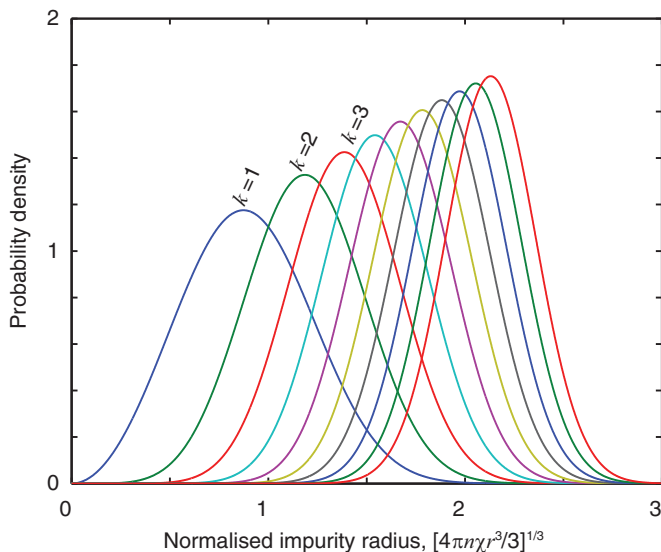


FIG. 18. (Color online) Probability distributions associated with the distance of a given spin to its first 10 nearest neighbors.

gives us an indication of how large the considered region may be (and hence the time scale) before NNN interactions become important. As we can see, for the case of a NV center coupled to a ^{13}C nuclear spin bath, where $T_2 < 1$ ms, we need only consider two-spin interactions.

In the above analysis, we have assumed that a given impurity may adopt any position within the environment, with the only constraint being the overall average density with which the impurities are distributed. However, as our primary focus is on the NV center in diamond, this is not strictly correct, as impurities may only occupy the atomic positions of a diamond cubic crystal structure.

Let $N(r)$ be the number of discrete lattice sites enclosed within a sphere of radius r , concentric on some impurity, and let $v_n \equiv v(r_n)$ denote the number of discrete lattice sites at radius r_n . Again invoking a binomial distribution, the probability of encountering the nearest-neighbor impurity 1 spin at radius r_n is the joint probability that one or more impurities reside at r_n and that there are no others within a sphere of this radius,

$$P_n = [1 - (1 - \chi)^{v_n}](1 - \chi)^{N_n - 1}. \quad (\text{B7})$$

The position vectors associated with the lattice sites in a cubic diamond unit cell of side length 4 are $\{\mathbf{u}_k\} = \{(0,0,0), (0,2,2)_{\odot}, (3,3,3), (3,1,1)_{\odot}\}$, where \odot denotes a cyclic permutation of vectorial components.

If we let $(l,m,n) \in \mathbb{N}^3$ index each individual cell, then the Cartesian coordinates of a given site are $\mathbf{U}_k = 4(l,m,n) + \mathbf{u}_k$. From this we find that the squared distance to the n th neighbor is $4n$ if n is even, and $4n - 1$ if n is odd. Both r_n and v_n are

given in Table II. Note that values of r_n^2 have been normalized, however, the distance between adjacent lattice sites is given by $l = 1.54 \text{ \AA}$.

This derivation of the discrete probability distribution allows us to determine the extent to which the continuum approximation is valid when computing ensemble averages of the various quantities that follow.

APPENDIX C: ENVIRONMENTAL AUTOCORRELATION FUNCTIONS AND FREQUENCY SPECTRA

In this section, we employ both the single-cluster autocorrelation functions derived in Sec. V corresponding to secular [Eq. (8)] and nonsecular [Eq. (9)] evolution of an individual cluster, together with the spatial statistics developed in the previous section (Appendix B), to determine the respective autocorrelation functions due to the sum of all clusters in the environment.

To obtain the correct short-time scaling of the secular function, we note that it is only the small clusters ($r \ll R_0$) that contribute to short-time dynamics of the system. The constituents of larger clusters communicate on much longer time scales and hence manifest as an effectively dc signal. Another way to think of this is to view the ensemble averages taken over the spatial distributions [Eq. (B3)] as a Fourier transform, with the conjugate (frequency) variable given by $\xi \equiv 3br^{-3}/2$. The short-time behavior ($t \ll 1/bn$) of the autocorrelation function therefore corresponds to the high-frequency behavior ($\xi \gg bn$) of the spectral distribution.

The secular autocorrelation function for a two-spin cluster is proportional to the difference in hyperfine couplings of the two nuclei. The leading-order behavior, corresponding to the high-frequency limit associated with smaller cluster sizes, comes from expanding these quantities for small r . In the ZSE regime, the magnitude of the fluctuating component only depends on the difference in the $z - z$ components of the respective hyperfine couplings

$$\begin{aligned} \Delta_z &= |A_{z,1} - A_{z,2}| \\ &\sim \frac{3ar}{R^4} \{ \sin(\theta) \sin(\Theta) [1 - 5 \cos^2(\Theta)] \cos(\phi - \Phi) \\ &\quad + \cos(\theta) \cos(\Theta) [3 - 5 \cos^2(\Theta)] \}, \end{aligned} \quad (\text{C1})$$

whereas in the SZE limit, this magnitude depends on all couplings to the axial component of the NV spin

$$\begin{aligned} \Delta &= \sqrt{A_{x,1}^2 + A_{y,1}^2 + A_{z,1}^2} - \sqrt{A_{x,2}^2 + A_{y,2}^2 + A_{z,2}^2} \\ &\sim \frac{1}{\sqrt{3 \cos^2(\Theta) + 1}} (4 \cos(\theta) \cos^3(\Theta) \\ &\quad + \sin(\theta) [2 \sin(\Theta) + \sin(3\Theta)] \cos(\phi - \Phi)). \end{aligned} \quad (\text{C2})$$

TABLE II. Table of normalized squared distances between crystal lattice sites, and the associated number of sites at that distance.

Neighbor	1	2	3	4	5	6	...	Odd n	Even n
$(\times l^2/3) r_n^2$	3	8	11	16	19	24	...	$4n - 1$	$4n$
v_n	4	12	12	6	12	24	...		

Employing these expansions and averaging over the spatial degrees of freedom using Eq. (B3), we find the collective autocorrelation function for the secular environment to be

$$\begin{aligned} & \langle \mathcal{B}_2(t)\mathcal{B}_2(0) \rangle_S \\ &= \frac{2}{5} \left(\frac{4}{3} \pi a n \right)^2 \left[4 + 6 \cos(\omega t) - \frac{1}{3} [7 \cos(\omega t) + 4] M(t) \right]. \end{aligned} \quad (\text{C3})$$

The function $M(t)$ is related to the secular magnetization, as given by

$$\begin{aligned} M(t) = & \frac{1}{3} \left\{ 3\Gamma\left(\frac{2}{3}\right) + \sqrt[6]{6}\pi^{11/6}(bnt)^{5/6} \left[(\sqrt{3}-3)\text{ber}_{\frac{5}{3}} \right. \right. \\ & \times \left(4\sqrt{\frac{\pi}{3}}\sqrt{bnt} \right) - (3+\sqrt{3})\text{bei}_{\frac{5}{3}} \left(4\sqrt{\frac{\pi}{3}}\sqrt{bnt} \right) \\ & + 2\sqrt{3}\text{bei}_{-\frac{5}{3}} \left(4\sqrt{\frac{\pi}{3}}\sqrt{bnt} \right) \\ & \left. \left. - 2\sqrt{3}\text{ber}_{-\frac{5}{3}} \left(4\sqrt{\frac{\pi}{3}}\sqrt{bnt} \right) \right] \right\}, \end{aligned} \quad (\text{C4})$$

where $\text{ber}(x)$ and $\text{bei}(x)$ are the Kelvin functions, defined by the real and imaginary parts of $J_\nu(xe^{3\pi i/4})$, respectively, and $J_\nu(x)$ is the ν th-order Bessel function of the first kind. This gives an autocorrelation time of

$$T_S = \frac{9}{4\pi^2 bn} \approx 9.6 \text{ ms}. \quad (\text{C5})$$

To leading order in t we have

$$M(t) \sim \frac{4\pi\sqrt[3]{6}}{\Gamma\left(\frac{8}{3}\right)} (\pi bnt)^{5/3} - \frac{8\pi}{\sqrt{3}\Gamma\left(\frac{4}{3}\right)} (\pi bnt)^2. \quad (\text{C6})$$

On the other hand, the collective autocorrelation function for the nonsecular environment may be computed exactly,

$$\langle \mathcal{B}_2(t)\mathcal{B}_2(0) \rangle_N = \frac{64}{9} \pi^2 a^2 n^2 [1 - N(t)]. \quad (\text{C7})$$

The function $N(t)$ is related to the collective nonsecular magnetization function, as given by

$$N(t) = \frac{2}{9} \left[\pi bnt \mathfrak{G}_{0,4}^{3,0} \left(\frac{1}{9} b^2 n^2 \pi^2 t^2 \middle| -\frac{1}{2}, 0, \frac{1}{2}, 0 \right) - 3 \right], \quad (\text{C8})$$

where \mathfrak{G} is the Meijer G function. To leading order, this results in a linear decay, given by

$$N(t) \sim \frac{4}{9} \pi^2 bnt, \quad (\text{C9})$$

with the same autocorrelation time as that of the secular autocorrelation function,

$$T_N = \frac{9}{4\pi^2 bn} \approx 9.6 \text{ ms}. \quad (\text{C10})$$

Having obtained the autocorrelation functions of the effective magnetic field, we can compute their Fourier transforms to give their corresponding spectral distributions. We do this by noticing that the role of the conjugate frequency variable is played by $\xi \equiv B = 3br^{-3}/2$. By transforming variables from r to ξ , we identify the secular and nonsecular spectral distributions to be

$$\begin{aligned} f_S(\xi) &= K_S \left(\frac{3b}{2\xi} \right)^{2/3} \frac{b}{2\xi^2} \exp\left(-\frac{2n\pi b}{\xi}\right), \\ f_N(\xi) &= K_N \frac{b}{2\xi^2} \exp\left(-\frac{2n\pi b}{\xi}\right), \end{aligned} \quad (\text{C11})$$

respectively, where K_S and K_N are normalization constants. The corresponding normalized spectra are plotted in Figs. 19(b) and 19(c). The lack of any significant spectral component near $\xi = 0$ is symptomatic of the cutoff imposed by the statistics associated with the size distribution of two-spin clusters. That is, since the exponential size cutoff associated with two-spin clusters prohibits arbitrarily large cluster sizes, there is no corresponding low-frequency region of the spectral density. Recall from the spatial statistics associated with higher-order cluster sizes [Eq. (B3)] that each successive k th neighbor introduces an associated probability distribution whose leading-order behavior scales as $r^{3k-1}/(k-1)!$. This, in turn, contributes an additional factor of $1/\xi$ to the spectral distribution for each successive order of clustering, with the modal frequencies occurring at

$$\overline{\xi_S^{(k)}} = \frac{2\pi nb}{k + \frac{5}{3}}, \quad \overline{\xi_N^{(k)}} = \frac{2\pi nb}{k + 1} \quad (\text{C12})$$

for the secular and nonsecular cases, respectively. Incorporation of successively higher orders of clustering will resolve the true low-frequency behaviour of the spectral distribution.

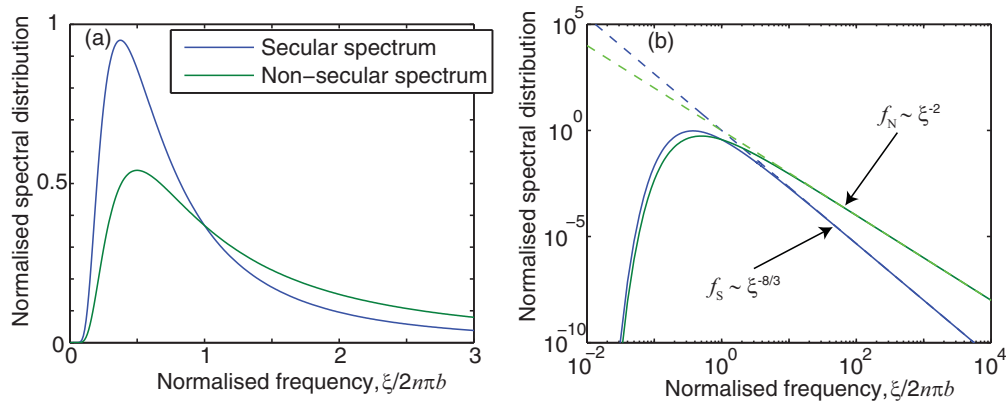


FIG. 19. (Color online) (a) Spectral distributions associated with the secular (blue) and nonsecular (green) spin-spin dynamics. (b) As in (a), but plotted on a log-log scale to show the high-frequency scaling of the spectra.

APPENDIX D: DECOHERENCE IN ULTRAPURE SINGLE-CRYSTAL DIAMOND

The determination of collective decoherence functions is performed by integrating the single-cluster decoherence functions (see Appendix A) over the $\mathbf{r} - \mathbf{R}$ domains as defined by the background field. Recall that the full spin-echo envelope is given by the product of all envelopes due to all clusters as weighted by the relevant spatial distributions

$$L = \prod_i L_i, \quad (\text{D1})$$

and taking the natural logarithm of both sides gives

$$\Lambda = - \sum_i \ln(L_i) \mapsto -\langle \ln(L_i) \rangle, \quad (\text{D2})$$

where the final line above denotes the ensemble average taken over all possible geometric cluster configurations. To compute these averages, we employ a formal expansion for the natural logarithm given by

$$\ln(1-x) = - \sum_{k=1}^{\infty} \frac{x^k}{k}, \quad (\text{D3})$$

which holds for $-1 \leq x < 1$. This condition is automatically satisfied since $-1 \leq L_{ZS}, L_{SZ} \leq 1$, and $0 \leq L_{ZSE}, L_{SZE}, L_{SEZ} \leq 1$. For example, in the ZSE case, we have

$$\Lambda_{ZSE} = \sum_{k=1}^{\infty} \frac{1}{k} \left[\sin^2 \left(\frac{Bt}{4} \right) \sin^2 \left(\frac{\Delta_z t}{4} \right) \right]^k. \quad (\text{D4})$$

However, we are only interested in the leading-order behavior of the ensemble-averaged decoherence function, to which all terms for $k \geq 2$ do not contribute.

1. Free-induction decay

To obtain the FID decoherence functions for the ZS and SZ regimes, we start with the single-spin decoherence function as given by Eq. (23). Integration over R gives

$$\int_l^{\infty} 4\pi n R^2 \Lambda_{ZS} dR = \frac{2}{3} \pi l^3 n \left[{}_1\mathfrak{F}_2 \left(-\frac{1}{2}; \frac{1}{2}, \frac{1}{2}; -\frac{a^2 t^2 [3 \cos(2\Theta) + 1]^2}{64 l^6} \right) - 1 \right], \quad (\text{D5})$$

$$\begin{aligned} \langle \Lambda_{ZSE} \rangle = & \frac{(-1)^{15/16} (\sqrt[4]{-1} - 1) \pi^{19/8} a_{\alpha}^{3/4} \sqrt[4]{bnt} \Gamma(-\frac{3}{4})}{16 \sqrt[8]{2} 3^{3/8}} (bnt)^{3/8} \left[(-1)^{3/8} + i \text{ber}_{-\frac{5}{4}} \left(2\sqrt{\frac{2\pi}{3}} \sqrt{bnt} \right) \right. \\ & + (\sqrt[8]{-1} + (-1)^{3/4}) \text{ber}_{\frac{5}{4}} \left(2\sqrt{\frac{2\pi}{3}} \sqrt{bnt} \right) + (1 + (-1)^{7/8}) \text{bei}_{-\frac{5}{4}} \left(2\sqrt{\frac{2\pi}{3}} \sqrt{bnt} \right) \\ & \left. + (\sqrt[4]{-1} + (-1)^{5/8}) \text{bei}_{\frac{5}{4}} \left(2\sqrt{\frac{2\pi}{3}} \sqrt{bnt} \right) \right] + \left(\frac{2\pi}{3} \right)^{3/4} \sin \left(\frac{\pi}{8} \right) \Gamma \left(\frac{5}{4} \right)^2 (a_{\alpha} n t)^{3/4}. \end{aligned} \quad (\text{D9})$$

Expanding this expression for $t \gg 1/an$ and $t \ll 1/bn$, and integrating over the angular degrees of freedom, gives the decoherence function for $t \sim T_2$ [Eq. (34)].

$$\int_l^{\infty} 4\pi n R^2 \Lambda_{SZ} dR = \frac{2}{3} \pi l^3 n \left[{}_1\mathfrak{F}_2 \left(-\frac{1}{2}; \frac{1}{2}, \frac{1}{2}; -\frac{a^2 t^2 [3 \cos(2\Theta) + 5]}{32 l^6} \right) - 1 \right], \quad (\text{D6})$$

where \mathfrak{F} is the generalized hypergeometric function. Expanding these expressions to leading order for short and long times, and integrating over the angular degrees of freedom gives the collective decoherence functions discussed in Sec. VI of the main text.

2. Spin-echo decoherence

We now move on to consideration of the spin-echo decoherence due to all spin clusters in the environment. Using Eq. (D3), the leading-order behavior of the decoherence functions for the ZSE, SZE, and SEZ regimes are given by

$$\begin{aligned} \langle \Lambda_{ZSE} \rangle & \sim \left\langle \sin^2 \left(\frac{Bt}{4} \right) \sin^2 \left(\frac{\Delta_z t}{4} \right) \right\rangle, \\ \langle \Lambda_{SZE} \rangle & \sim \left\langle \sin^2 \left(\frac{Bt}{4} \right) \sin^2 \left(\frac{\Delta t}{4} \right) \right\rangle, \\ \langle \Lambda_{SEZ} \rangle & \sim \left\langle \frac{8}{15} \sin^2 \left(\frac{3Bt}{4} \right) \left[\sin^2 \left(\frac{At}{2} \right) + \sin^2 \left(\frac{At}{4} \right) \right] \right\rangle, \end{aligned} \quad (\text{D7})$$

respectively.

a. Spin-echo decay at high magnetic fields (ZSE)

As the spin-echo decoherence times are much shorter than the environmental correlation times, we may expand Δ_z for small r , giving

$$\begin{aligned} \Delta_z & \sim \frac{3ar}{R^4} [\sin(\theta) \sin(\Theta) [1 - 5 \cos^2(\Theta)] \cos(\phi - \Phi) \\ & + \cos(\theta) \cos(\Theta) [3 - 5 \cos^2(\Theta)]] \equiv \frac{a_{\alpha} r}{R^4}. \end{aligned} \quad (\text{D8})$$

To obtain the ZSE decoherence function in the long-time limit, we integrate $\langle \Lambda_{ZSE} \rangle$ [Eq. (D7)] over the spatial degrees of freedom R and r , using Eq. (B3), giving

To obtain the behavior of the decoherence function at intermediate times, we must make a correction for the diamond bond length to the nuclear-nuclear component of the evolution,

while integrating over the hyperfine dynamics as above. The associated integral is generally intractable for arbitrary limits of r , however, as $l \ll n^{-1/3}$ we may approximate the probability distribution (B3) by its leading-order behavior $P(r) \sim 4\pi nr^2$, giving

$$\begin{aligned} \langle \Lambda_{\text{ZSE}} \rangle &\sim \left(\int_0^\infty P(r) - \int_0^l 4\pi r^2 \right) \frac{2\pi n}{3} \sin\left(\frac{\pi}{8}\right) \Gamma\left(\frac{1}{4}\right) \\ &\quad \times \left(\frac{a_\alpha r t}{2} \right)^{3/4} \sin^2\left(\frac{3Bt}{4}\right) dr \\ &= \frac{\pi^2}{20} \sqrt{2(\sqrt{2}-1)} l^{15/4} n^2 \Gamma\left(\frac{1}{4}\right) (at)^{3/4} \\ &\quad \times \left[{}_1\mathfrak{F}_2\left(-\frac{5}{8}; \frac{3}{8}, \frac{1}{2}; -\frac{b^2 t^2}{16l^6}\right) - 1 \right]. \end{aligned} \quad (\text{D10})$$

Expanding this expression for $t \gg 1/an$ and $t \ll 1/bn$ gives the expression for the ZSE decoherence function at intermediate times [Eq. (36)].

To obtain the behavior of the decoherence function at short times, we make a similar adjustment for the bond length in the hyperfine interaction, and then expand for $t \ll 1/an$ and $t \ll 1/bn$, as given by Eq. (37) of the main text.

b. Spin-echo decay at moderate magnetic fields (SZE)

The procedure to compute the ensemble-averaged decoherence function in the SZE regime is the same as that for the ZSE regime, however, we make the substitution $\Delta_z \mapsto \Delta$, leading to what is essentially a redefinition of a_α :

$$\begin{aligned} a_\alpha \mapsto &\frac{1}{\sqrt{3 \cos^2(\Theta) + 1}} (4 \cos(\theta) \cos^3(\Theta) + \sin(\theta) [2 \sin(\Theta) \\ &+ \sin(3\Theta)] \cos(\phi - \Phi)). \end{aligned} \quad (\text{D11})$$

Following this redefinition, the computation of decoherence functions in the SZE regime is the same as that for the ZSE regime.

c. Spin-echo decay at low magnetic fields (SEZ)

To obtain the analytic limits of the SEZ decoherence function, we follow the same progression as in the ZSE and SZE limits above. The SEZ limit is somewhat simpler, however, owing to the fact that the hyperfine and dipole-dipole processes are decoupled from one another in the single-cluster SEZ decoherence function [Eq. (D7)]. Integration over the hyperfine component from $l < R < \infty$ yields

$$\begin{aligned} &\int_l^\infty \left[\sin^2\left(\frac{At}{2}\right) + \sin^2\left(\frac{At}{4}\right) \right] R^2 dR \\ &= \frac{2}{3} n \left\{ l^3 \left[{}_1\mathfrak{F}_2\left(-\frac{1}{2}; \frac{1}{2}, \frac{1}{2}; -\frac{a^2 t^2}{16l^6}\right) \right. \right. \\ &\quad \left. \left. + \cos\left(\frac{at}{l^3}\right) - 2 \right] + at \text{Si}\left(\frac{at}{l^3}\right) \right\}. \end{aligned} \quad (\text{D12})$$

Integration over r from l to ∞ in the dipolar interaction gives

$$\begin{aligned} &\int_l^\infty P(r) \sin^2\left(\frac{3Bt}{4}\right) dr \\ &= \frac{1}{4} \left[2 - \pi bnt \mathfrak{E}_{0,4}^{3,0}\left(\frac{b^2 n^2 \pi^2 t^2}{4} \middle| -\frac{1}{2}, 0, \frac{1}{2}, 0\right) \right] \\ &\quad - \frac{1}{6} \pi n \left[-6bt \text{Si}\left(\frac{3bt}{2l^3}\right) - 4l^3 \cos\left(\frac{3bt}{2l^3}\right) \right. \\ &\quad \left. + 3\pi bt + 4l^3 \right], \end{aligned} \quad (\text{D13})$$

where Si is the sine integral function, defined by $\text{Si}(x) = \int_0^x t^{-1} \sin(t) dt$. Taking the relevant limits of the dipolar and hyperfine components, integrating over the angular degrees of freedom, and substituting into the definition of $\langle \Lambda_{\text{SEZ}} \rangle$ [Eq. (D7)], we find the long-, intermediate-, and short-time limits of the SEZ decoherence to be as given in Eqs. (39)–(41), respectively.

APPENDIX E: ON THE QUESTION OF WHETHER THE QUANTUM SPIN BATH MAY BE MODELED AS A CLASSICAL MAGNETIC FIELD

The time-evolution operator for a spin-echo experiment is

$$\mathcal{U} = \mathcal{U}_f(t/2, t) \mathcal{F} \mathcal{U}_f(0, t/2), \quad (\text{E1})$$

and for an arbitrary pulse sequence with pulses applied at $t_k = \{t_1, t_2, \dots, t_n\}$, we have

$$\begin{aligned} \mathcal{U}(t) &= \mathcal{U}(t_n, t) \mathcal{F} \dots \mathcal{F} \mathcal{U}(t_1, t_2) \mathcal{F} \mathcal{U}(0, t_1) \\ &\equiv e^{-i\phi_1} |1\rangle \langle 1| + e^{-i\phi_0} |0\rangle \langle 0|, \end{aligned} \quad (\text{E2})$$

where

$$\begin{aligned} \phi_1 &= \phi(0, t_1) + \phi(t_2, t_3) + \dots, \\ \phi_0 &= \phi(t_1, t_2) + \phi(t_3, t_4) + \dots \end{aligned} \quad (\text{E3})$$

are the accumulated phases of the $|1\rangle$ and $|0\rangle$ states, respectively.

Using this semiclassical approach for an initial probe spin state of $|\psi_0\rangle = \frac{1}{\sqrt{2}}(|0\rangle + |1\rangle)$, we find the in-plane projection of the magnetization to be

$$\begin{aligned} L &= \text{Tr}\{(\mathcal{S}_x + i\mathcal{S}_y) \mathcal{U}(t) \rho_0 \mathcal{U}^\dagger(t)\} \\ &= \frac{1}{2} \exp[i[\phi_1^*(t) - \phi_0(t)]]. \end{aligned}$$

This quantity is an average over the quantum degrees of freedom in the system, but we have not yet addressed the statistics of the field B . First, we note that the amplitude of $B(t)$ at any given t is a sum over a large number of sources and is therefore normally distributed. Furthermore, at room temperature, thermal energies are much larger than the coupling of environmental spins to static background fields $k_B T \gg \omega \sqrt{S(S+1)}$, implying that $\langle B \rangle = 0$ and hence $\langle \varphi \rangle = 0$. To compute the ensemble average $\langle S \rangle$, we make

the substitution to the normally distributed variable $\varphi = \phi_1^*(t) - \phi_0(t)$, which, by definition, has standard deviation $\sqrt{\langle\varphi^2\rangle - \langle\varphi\rangle^2}$, giving $\langle S \rangle = \frac{1}{2} \exp(-\frac{1}{2}\langle\varphi^2\rangle)$ where

$$\varphi = \sum_{k=0} \left[\int_{t_{2k}}^{t_{2k+1}} - \int_{t_{2k+1}}^{t_{2k+2}} \right] B(t') dt' \quad (\text{E4})$$

and

$$\langle\varphi^2\rangle = \sum_{k=0} \sum_{j=0} \left[\int_{t_{2k}}^{t_{2k+1}} dt' - \int_{t_{2k+1}}^{t_{2k+2}} dt' \right] \left[\int_{t_{2j}}^{t_{2j+1}} dt'' - \int_{t_{2j+1}}^{t_{2j+2}} dt'' \right] \langle B(t') B(t'') \rangle. \quad (\text{E5})$$

We therefore define the semiclassical analog of the decoherence function Λ via

$$\Lambda \equiv \frac{1}{2} \langle\varphi^2\rangle. \quad (\text{E6})$$

The problem of determining Λ then reduces to finding an expression for the autocorrelation function of the effective magnetic field, as was detailed in Appendices A and C.

-
- [1] J. Preskill, *Proc. R. Soc. London, Ser. A* **454**, 385 (1998).
[2] D. Loss and D. P. DiVincenzo, *Phys. Rev. A* **57**, 120 (1998).
[3] R.-B. Liu, W. Yao, and L. J. Sham, *Adv. Phys.* **59**, 703 (2010).
[4] B. E. Kane, *Nature (London)* **393**, 133 (1998).
[5] R. de Sousa, J. D. Delgado, and S. Das Sarma, *Phys. Rev. A* **70**, 052304 (2004).
[6] L. C. L. Hollenberg, A. D. Greentree, A. G. Fowler, and C. J. Wellard, *Phys. Rev. B* **74**, 045311 (2006).
[7] J. J. L. Morton and B. W. Lovett, in *Hybrid Solid-State Qubits: The Powerful Role of Electron Spins*, Vol. 2 of Annual Review of Condensed Matter Physics (Annual Reviews, Palo Alto, CA, 2011), pp. 189–212.
[8] J. Wrachtrup and F. Jelezko, *J. Phys.: Condens. Matter* **18**, 115303 (2006).
[9] C. L. Degen, *Appl. Phys. Lett.* **92**, 243111 (2008).
[10] J. M. Taylor, P. Cappellaro, L. Childress, L. Jiang, D. Budker, P. R. Hemmer, A. Yacoby, R. Walsworth, and M. D. Lukin, *Nat. Phys.* **4**, 810 (2008).
[11] G. Balasubramanian, I. Y. Chan, R. Kolesov, M. Al-Hmoud, J. Tisler, C. Shin, C. Kim, A. Wojcik, P. R. Hemmer, A. Krueger *et al.*, *Nature (London)* **455**, 648 (2008).
[12] J. R. Maze, P. L. Stanwix, J. S. Hodges, S. Hong, J. M. Taylor, P. Cappellaro, L. Jiang, M. V. G. Dutt, E. Togan, A. S. Zibrov *et al.*, *Nature (London)* **455**, 644 (2008).
[13] L. T. Hall, C. D. Hill, J. H. Cole, and L. C. L. Hollenberg, *Phys. Rev. B* **82**, 045208 (2010).
[14] T. Staudacher, F. Shi, S. Pezzagna, J. Meijer, J. Du, C. A. Meriles, F. Reinhard, and J. Wrachtrup, *Science* **339**, 561 (2013).
[15] H. J. Mamin, M. Kim, M. H. Sherwood, C. T. Rettner, K. Ohno, D. D. Awschalom, and D. Rugar, *Science* **339**, 557 (2013).
[16] V. S. Perunicic, L. T. Hall, D. A. Simpson, C. D. Hill, and L. C. L. Hollenberg, *Phys. Rev. B* **89**, 054432 (2014).
[17] L. T. Hall, C. D. Hill, J. H. Cole, B. Stadler, F. Caruso, P. Mulvaney, J. Wrachtrup, and L. C. L. Hollenberg, *Proc. Natl. Acad. Sci. USA* **107**, 18777 (2010).
[18] L. P. McGuinness, Y. Yan, A. Stacey, D. A. Simpson, L. T. Hall, D. Maclaurin, S. Praver, P. Mulvaney, J. Wrachtrup, F. Caruso *et al.*, *Nat. Nanotechnol.* **6**, 358 (2011).
[19] L. T. Hall, G. C. G. Beart, E. A. Thomas, D. A. Simpson, L. P. McGuinness, J. H. Cole, J. H. Manton, R. E. Scholten, F. Jelezko, J. Wrachtrup *et al.*, *Sci. Rep.* **2**, 9 (2012).
[20] F. Dolde, H. Fedder, M. W. Doherty, T. Nobauer, F. Remppe, G. Balasubramanian, T. Wolf, F. Reinhard, L. C. L. Hollenberg, F. Jelezko *et al.*, *Nat. Phys.* **7**, 459 (2011).
[21] P. Neumann, I. Jakobi, F. Dolde, C. Burk, R. Reuter, G. Waldherr, J. Honert, T. Wolf, A. Brunner, J. H. Shim *et al.*, *Nano Lett.* **13**, 2738 (2013).
[22] H. C. Jared and C. L. H. Lloyd, *Nanotechnology* **20**, 495401 (2009).
[23] L. T. Hall, J. H. Cole, C. D. Hill, and L. C. L. Hollenberg, *Phys. Rev. Lett.* **103**, 220802 (2009).
[24] S. Steinert, F. Ziem, L. T. Hall, A. Zappe, M. Schweikert, N. Gotz, A. Aird, G. Balasubramanian, L. Hollenberg, and J. Wrachtrup, *Nat. Commun.* **4**, 1607 (2013).
[25] S. Kaufmann, D. A. Simpson, L. T. Hall, V. Perunicic, P. Senn, S. Steinert, L. P. McGuinness, B. C. Johnson, T. Ohshima, F. Caruso *et al.*, *Proc. Natl. Acad. Sci. USA* **110**, 10894 (2013).
[26] L. P. McGuinness, L. T. Hall, A. Stacey, D. A. Simpson, C. D. Hill, J. H. Cole, K. Ganesan, B. C. Gibson, S. Praver, P. Mulvaney *et al.*, *New J. Phys.* **15**, 073042 (2013).
[27] R. de Sousa and S. Das Sarma, *Phys. Rev. B* **67**, 033301 (2003).
[28] R. de Sousa and S. Das Sarma, *Phys. Rev. B* **68**, 115322 (2003).
[29] R. Hanson, V. V. Dobrovitski, A. E. Feiguin, O. Gywat, and D. D. Awschalom, *Science* **320**, 352 (2008).
[30] J. R. Maze, J. M. Taylor, and M. D. Lukin, *Phys. Rev. B* **78**, 094303 (2008).
[31] V. V. Dobrovitski, A. E. Feiguin, R. Hanson, and D. D. Awschalom, *Phys. Rev. Lett.* **102**, 237601 (2009).
[32] G. de Lange, Z. H. Wang, D. Riste, V. V. Dobrovitski, and R. Hanson, *Science* **330**, 60 (2010).
[33] G. de Lange, D. Riste, V. V. Dobrovitski, and R. Hanson, *Phys. Rev. Lett.* **106**, 080802 (2011).
[34] Z.-H. Wang, G. de Lange, D. Ristè, R. Hanson, and V. V. Dobrovitski, *Phys. Rev. B* **85**, 155204 (2012).
[35] W. M. Witzel, R. de Sousa, and S. Das Sarma, *Phys. Rev. B* **72**, 161306 (2005).

- [36] W. M. Witzel and S. Das Sarma, *Phys. Rev. B* **74**, 035322 (2006).
- [37] S. K. Saikin, W. Yao, and L. J. Sham, *Phys. Rev. B* **75**, 125314 (2007).
- [38] W. Yao, R.-B. Liu, and L. J. Sham, *Phys. Rev. B* **74**, 195301 (2006).
- [39] W. Yao, R.-B. Liu, and L. J. Sham, *Phys. Rev. Lett.* **98**, 077602 (2007).
- [40] L. Ren-Bao, Y. Wang, and L. J. Sham, *New J. Phys.* **9**, 226 (2007).
- [41] W. Yang and R.-B. Liu, *Phys. Rev. B* **78**, 085315 (2008).
- [42] W. Yang and R.-B. Liu, *Phys. Rev. B* **79**, 115320 (2009).
- [43] M. W. Doherty, N. B. Manson, P. Delaney, F. Jelezko, J. Wrachtrup, and L. C. L. Hollenberg, *Phys. Rep.* **528**, 1 (2013).
- [44] F. Jelezko, I. Popa, A. Gruber, C. Tietz, J. Wrachtrup, A. Nizovtsev, and S. Kilin, *Appl. Phys. Lett.* **81**, 2160 (2002).
- [45] F. Jelezko and J. Wrachtrup, *Phys. Status Solidi A* **203**, 3207 (2006).
- [46] F. Jelezko, T. Gaebel, I. Popa, A. Gruber, and J. Wrachtrup, *Phys. Rev. Lett.* **92**, 076401 (2004).
- [47] P. W. Anderson and P. R. Weiss, *Rev. Mod. Phys.* **25**, 269 (1953).
- [48] J. R. Klauder and P. W. Anderson, *Phys. Rev.* **125**, 912 (1962).
- [49] R. de Sousa, in *Electron Spin as a Spectrometer of Nuclear-Spin Noise and Other Fluctuations*, Vol. 115 of Topics in Applied Physics (Springer, Berlin, 2009), pp. 183–220.
- [50] B. Lee, W. M. Witzel, and S. Das Sarma, *Phys. Rev. Lett.* **100**, 160505 (2008).
- [51] L. Cywinski, R. M. Lutchyn, C. P. Nave, and S. Das Sarma, *Phys. Rev. B* **77**, 174509 (2008).
- [52] S. U. Gtz, *New J. Phys.* **10**, 083024 (2008).
- [53] G. Balasubramanian, P. Neumann, D. Twitchen, M. Markham, R. Kolesov, N. Mizuochi, J. Isoya, J. Achard, J. Beck, J. Tissler *et al.*, *Nat. Mater.* **8**, 383 (2009).
- [54] L. Cywinski, W. M. Witzel, and S. Das Sarma, *Phys. Rev. B* **79**, 245314 (2009).
- [55] L. Cywinski, W. M. Witzel, and S. Das Sarma, *Phys. Rev. Lett.* **102**, 057601 (2009).
- [56] L. Cywinski, V. V. Dobrovitski, and S. Das Sarma, *Phys. Rev. B* **82**, 035315 (2010).
- [57] E. Barnes, L. Cywinski, and S. Das Sarma, *Phys. Rev. B* **84**, 155315 (2011).
- [58] E. Barnes, L. Cywinski, and S. Das Sarma, *Phys. Rev. Lett.* **109**, 140403 (2012).
- [59] N. Zhao, S.-W. Ho, and R.-B. Liu, *Phys. Rev. B* **85**, 115303 (2012).
- [60] W. M. Witzel, M. S. Carroll, Ł. Cywiński, and S. Das Sarma, *Phys. Rev. B* **86**, 035452 (2012).
- [61] S. Steinert, F. Dolde, P. Neumann, A. Aird, B. Naydenov, G. Balasubramanian, F. Jelezko, and J. Wrachtrup, *Rev. Sci. Instrum.* **81**, 043705 (2010).
- [62] V. V. Dobrovitski, A. E. Feiguin, D. D. Awschalom, and R. Hanson, *Phys. Rev. B* **77**, 245212 (2008).
- [63] J. R. Maze, A. Drau, V. Waselowski, H. Duarte, J. F. Roch, and V. Jacques, *New J. Phys.* **14**, 103041 (2012).
- [64] L. Childress, M. V. Gurudev Dutt, J. M. Taylor, A. S. Zibrov, F. Jelezko, J. Wrachtrup, P. R. Hemmer, and M. D. Lukin, *Science* **314**, 281 (2006).